

## THE DISTRIBUTION OF ULTRA-DIFFUSE AND ULTRA-COMPACT GALAXIES IN THE FRONTIER FIELDS

STEVEN R. JANSSENS<sup>1</sup>, ROBERTO ABRAHAM<sup>1</sup>, JEAN BRODIE<sup>2</sup>, DUNCAN A. FORBES<sup>3</sup>, AND AARON J. ROMANOWSKY<sup>2,4</sup>*Draft version August 21, 2021*

## ABSTRACT

Large low surface brightness galaxies have recently been found to be abundant in nearby galaxy clusters. In this paper, we investigate these ultra-diffuse galaxies (UDGs) in the six *Hubble* Frontier Fields galaxy clusters: Abell 2744, MACSJ0416.1–2403, MACSJ0717.5+3745, MACSJ1149.5+2223, Abell S1063 and Abell 370. These are the most massive ( $1\text{--}3 \times 10^{15} M_{\odot}$ ) and distant ( $0.308 < z < 0.545$ ) systems in which this class of galaxy has yet been discovered. We estimate that the clusters host of the order of  $\sim 200\text{--}1400$  UDGs inside the virial radius ( $R_{200}$ ), consistent with the UDG abundance halo-mass relation found in the local universe, and suggests that UDGs may be formed in clusters. Within each cluster, however, we find that UDGs are not evenly distributed. Instead their projected spatial distributions are lopsided, and they are deficient in the regions of highest mass density as traced by gravitational lensing. While the deficiency of UDGs in central regions is not surprising, the lopsidedness is puzzling. The UDGs, and their lopsided spatial distributions, may be associated with known substructures late in their infall into the clusters, meaning that we find evidence both for formation of UDGs in clusters and for UDGs falling into clusters. We also investigate the ultra-compact dwarfs (UCDs) residing in the clusters, and find the spatial distributions of UDGs and UCDs appear anti-correlated. Around 15% of UDGs exhibit either compact nuclei or nearby point sources. Taken together, these observations provide additional evidence for a picture in which at least some UDGs are destroyed in dense cluster environments and leave behind a residue of UCDs.

*Keywords:* galaxies: clusters: general – galaxies: dwarf – galaxies: general

## 1. INTRODUCTION

Large low surface brightness galaxies in galaxy clusters were first reported by Sandage & Binggeli (1984) who noted the existence of “very-large-size, low-surface-brightness dwarfs” in the Virgo cluster. They chose not to introduce a new morphological designation for these galaxies, since apart from their large sizes ( $\sim 10$  kpc in diameter), they resemble otherwise normal dwarfs or dwarf irregulars (Binggeli et al. 1985). Similarly, Impey et al. (1988) found an additional 27 examples in Virgo, and similar large low surface brightness galaxies were found in Fornax (Ferguson, & Sandage 1988; Bothun et al. 1991). Related objects were also found in lower density environments, such as the low surface brightness galaxies described by Dalcanton et al. (1997), and F8D1 in the M81 group (Caldwell et al. 1998).

The interest in large low-surface-brightness galaxies has recently been reignited by the discovery of the enormous abundance of such ‘extreme’ low surface brightness systems in the richest environments, most notably the discovery of very large numbers of such systems in the Coma cluster (see van Dokkum et al. 2015; Koda et al. 2015), coupled with the remarkable properties of the small number of such objects that have been investigated in detail by follow-up investigations (e.g. Beasley et al. 2016; van Dokkum et al. 2016, 2018; Danieli et al. 2019;

van Dokkum et al. 2019a; Martín-Navarro et al. 2019). At least a subset of such objects appear to host very extensive globular cluster systems and exhibit anomalous dynamical mass-to-light ratios (described in greater detail below). As a result of this, and following a suggestion by van Dokkum et al. (2015), very large low-surface brightness galaxies in clusters have come to be known as ‘ultra-diffuse galaxies’ (UDGs).

There is no universally accepted definition of a UDG in the literature. Slight differences arise from the variety of instruments and techniques used (Martin et al. 2019). However, they are typically defined in morphological terms as very extended stellar systems with large effective radii ( $R_e \gtrsim 1.5$  kpc), low Sérsic indices ( $n \lesssim 1.5$ ), and characteristic surface brightnesses fainter than  $\sim 24$  mag arcsec<sup>−2</sup>, i.e. roughly Milky Way sized with  $1/100\text{--}1/1000$  the stellar mass. van Dokkum et al. (2015) chose to adopt the central surface brightness of UDGs as the characteristic surface brightness of the class, and required this to be fainter than  $\mu_{0,g} \approx 24$  mag arcsec<sup>−2</sup>. On the other hand, Koda et al. (2015) adopted the mean surface-brightness inside  $R_e$  in the  $R$ -band as the characteristic surface brightness, and defined their sample using a cut of  $\langle \mu \rangle_{e,R} > 24$  mag arcsec<sup>−2</sup>. Concentrated, likely background, systems were removed by requiring  $\langle \mu \rangle_e$  to not significantly deviate from the surface brightness at  $R_e$ . Similarly, van der Burg et al. (2016) used an  $r$ -band surface brightness cut of  $\langle \mu \rangle_{e,r} \geq 24$  mag arcsec<sup>−2</sup> and removed concentrated systems with a Sérsic index cut of  $n \leq 4$ .

UDGs appear to be quenched systems and occupy the red sequence in clusters (van Dokkum et al. 2015; van der Burg et al. 2016), although UDG-like systems in the field are typically bluer (e.g. Leisman et al. 2017; Román,

janssens@astro.utoronto.ca

<sup>1</sup> Department of Astronomy and Astrophysics, University of Toronto, 50 St. George Street, Toronto, ON, Canada M5S 3H4<sup>2</sup> University of California Observatories, 1156 High Street, Santa Cruz, CA 95064, USA<sup>3</sup> Centre for Astrophysics and Supercomputing, Swinburne University, Hawthorn VIC 3122, Australia<sup>4</sup> Department of Physics and Astronomy, San José State University, One Washington Square, San Jose, CA 95192, USA

& Trujillo 2017b). The axial ratios of UDGs in Coma are consistent with being prolate shaped, with a mean axial ratio of  $\sim 0.7$  and very few with axial ratios less than 0.4 (Burkert 2017, but see Rong et al. 2019). This, along with their low  $V_{\text{rot}}/\sigma$  (van Dokkum et al. 2019b), suggests that UDGs are dispersion-dominated systems and not rotationally supported thick disks, and are perhaps related to the lower mass low surface brightness dwarf spheroidals in the Local Group (Burkert 2017).

It was first proposed that UDGs are “failed”  $L^*$  galaxies after having lost their gas supply in early times and are now extremely dark matter dominated, allowing them to survive in such dense environments (van Dokkum et al. 2015). Two objects in Coma, Dragonfly 17 and Dragonfly 44, and one in Virgo, VCC 1287, are possible examples of such a scenario. Dragonfly 17 hosts  $\sim 30$  globular clusters (GCs), which is abnormally high for its luminosity, suggesting it could possibly be a “failed” M33- or LMC-like galaxy (Peng & Lim 2016; Beasley, & Trujillo 2016). VCC 1287 is similarly a possibly failed LMC-like galaxy based on its GC system (Beasley et al. 2016). Dragonfly 44 is much more massive, with  $\sim 75$  GCs and a dynamical mass consistent with being a failed Milky Way-like system (van Dokkum et al. 2016, 2019b). Subsequent investigations, however, suggest that many UDGs have stellar masses and dark matter halos consistent with dwarf galaxies, suggesting Dragonfly 44 may be an extreme case (Beasley et al. 2016; Peng & Lim 2016; Amorisco et al. 2018; Alabi et al. 2018; Ferré-Mateu et al. 2018). At the other extreme, two UDGs in the NGC 1052 group, NGC1052-DF2 and NGC1052-DF4, have very low velocity dispersions and dynamical masses consistent with little or no dark matter (van Dokkum et al. 2018, 2019a; Danieli et al. 2019).

With such a range of properties exhibited by UDGs, the low surface brightness universe is proving to be just as diverse as the high surface brightness universe. Numerous formation channels have been brought forward to create such an array of objects. In the failed massive halo scenario, possible mechanisms that could remove the gas and prevent the formation of a normal stellar population include extreme feedback from supernovae and young stars (Agertz, & Kravtsov 2016; Di Cintio et al. 2017; Chan et al. 2018), ram pressure stripping (Yozin & Bekki 2015; Jiang et al. 2019; Tremmel et al. 2019) or AGN feedback (Reines et al. 2013). With these likely being extreme examples however, other mechanisms may also be in play to form UDGs within lower mass dark matter halos. If UDGs are “inflated dwarfs”, both dark matter halos with anomalously high spins (Amorisco & Loeb 2016; Rong et al. 2017; Liao et al. 2019) and tidal interactions (Yozin & Bekki 2015; Jiang et al. 2019; Liao et al. 2019; Martin et al. 2019; Sales et al. 2019) may be responsible for their large sizes. Rare UDGs without dark matter may be the result of high-velocity collisions of dwarfs in protogroup environments (Silk 2019). Furthermore, the near-linear relation between the abundance of UDGs and cluster halo mass (van der Burg et al. 2016; Román, & Trujillo 2017b; van der Burg et al. 2017; Janssens et al. 2017; Mancera Piña et al. 2018), in addition to their existence in low density environments, suggests an ‘internal’ mechanism of UDG formation that is independent of environment, and that UDGs are a consistent fraction of the galaxy population in all environ-

ments (Amorisco et al. 2018).

At the other extreme of low stellar mass galaxies lie the ‘ultra-compact dwarfs’ (UCDs). With characteristic luminosities  $\gtrsim 10^7 L_{\odot}$  and radii  $r_h \gtrsim 10$  pc, they resemble both the nuclei of low-mass galaxies and the most massive GCs (Brodie et al. 2011; Norris et al. 2014; Forbes et al. 2014; Janz et al. 2016). As they are typically found in the densest environments, environmental effects, such as tidal stripping, are thought to be involved in their formation (Bekki et al. 2003; Pfeffer & Baumgardt 2013).

In a previous paper, we looked at the UDGs and UCDs in Abell 2744 (Janssens et al. 2017), the first cluster observed by the Frontier Fields (FF) program with the *Hubble Space Telescope* (*HST*). In this paper, we now investigate the UDGs and UCDs inhabiting all six FF galaxy clusters. In addition to being the most massive and distant systems in which UDGs have yet been discovered, the existing lensing and X-ray analyses permit detailed study of their local environments. This paper is organized as follows. In Section 2, we describe the FF program and its data. Our methods, including UDG and UCD selection, are described in Section 3. In Section 4, we present and discuss the results of our analysis, primarily the abundance of UDGs in the six FF clusters and their spatial distributions in relation to other classes of galaxies and known substructures in the clusters.

We adopt a  $\Lambda$ CDM cosmology with  $\Omega_m = 0.3$ ,  $\Omega_{\Lambda} = 0.7$ ,  $H_0 = 70 \text{ km s}^{-1} \text{ Mpc}^{-1}$ . All magnitudes are in the AB system. Galactic extinction corrections from the Schlafly & Finkbeiner (2011) extinction maps were applied to all colours and magnitudes.<sup>5</sup>

## 2. DATA

The *HST* FF program has produced the deepest images to date of galaxy clusters and gravitationally lensed galaxies for six high-magnification clusters—Abell 2744, MACSJ0416.1–2403, MACSJ0717.5+3745, MACSJ1149.5+2223, Abell S1063 (also known as RXCJ2248.7–4431) and Abell 370—along with six corresponding parallel “blank” fields offset  $\sim 6'$  from each cluster (Lotz et al. 2017). These clusters were chosen for their known high lensing strengths, low sky backgrounds and Galactic extinctions, in addition to observability with *HST*, *Spitzer* and ground-based facilities (Lotz et al. 2017). Selecting galaxy clusters for their lensing strength will end up selecting extremely massive, merging clusters, as the merger stretches the lensing critical curves between the various components resulting in relatively large areas subject to high magnification (Redlich et al. 2012; Diego et al. 2016). The cluster properties are summarized in Table 1. The coordinates are the cluster centres as defined by their stellar content, that is the location of the brightest cluster galaxy (BCG), or where the cluster is comprised of multiple merging subclusters, the centroid of the BCGs. The diverse and complex morphologies displayed by these clusters is discussed later. Each cluster and parallel field pair was observed for 70 orbits with the Advanced Camera for Surveys Wide Field Camera (ACS/WFC) in *F*435W, *F*606W and *F*814W, and 70 orbits with the Wide Field Camera 3 IR channel (WFC3/IR) in *F*105W, *F*125W, *F*140W and *F*160W,

<sup>5</sup> Using the online calculator at <https://ned.ipac.caltech.edu/forms/calculator.html>.

achieving  $5\sigma$  depths of  $\sim 29$ th AB magnitude (Lotz et al. 2017).

Despite the  $\sim 6'$  separations between the cluster and parallel fields, the parallel fields are still either within or straddle the virial radii ( $R_{200}$ ) of the clusters and so these images are examined for UDGs as well. To estimate the contamination of our UDG sample by background galaxies, we instead use the eXtreme Deep Field (XDF, Illingworth et al. 2013). This is the only image of the sky that is deeper than the FFs to date, and was obtained by stacking the data from 19 different *HST* programs completed between 2002 and 2012 covering the *Hubble* Ultra Deep Field (Illingworth et al. 2013). The XDF has ACS/WFC coverage in  $F435W$ ,  $F606W$ ,  $F775W$ ,  $F814W$  and  $F850LP$ , and WFC3/IR coverage in  $F105W$ ,  $F125W$ ,  $F140W$  and  $F160W$ .

### 3. METHODOLOGY

#### 3.1. Source detection

For each of the six FF clusters, SEXTRACTOR (Bertin & Arnouts 1996) was run in dual image mode on the 30 mas images of both the cluster core and parallel fields. The  $F814W$  image was used as the detection image for all bands. A WEIGHT\_THRESH of 0.002 was used to remove sources detected in the low exposure time regions along the edges of the fields. The XDF was treated similarly. In Janssens et al. (2017), we used the  $F775W$  image as the XDF detection image since it is much deeper than the XDF  $F814W$  image. However, the XDF  $F814W$  image is of comparable depth to the FF  $F814W$  images, and its use simplifies the background correction while having no effect on the results. Only 60 mas WFC3/IR images are available for the XDF so a second 60 mas multiband catalog was created for the XDF, matched to the 30 mas catalog, and used only for WFC3/IR colours.

#### 3.2. Structural parameters

GALFIT (Peng et al. 2002) was used to determine  $I_{814}$ -band structural parameters by fitting a single component Sérsic model to the  $F814W$  image of every object brighter than  $F814W = 28$  mag with SEXTRACTOR FLAGS < 4 in the catalogs.

We used PSFEX (Bertin 2011) to supply GALFIT with point spread functions (PSFs) for each object. For each image, a sample of point sources was selected from a shallower SEXTRACTOR catalog with the cuts  $1.0 < \text{FWHM} < 10.0$  pixels, signal-to-noise ratio  $\geq 5$  and ellipticity  $e < 0.3$ . A cubic polynomial was used to map the variability of the PSF across the image.

Similar to van der Wel et al. (2012), the provided reduced images and RMS maps were combined to produce total noise maps to pass to GALFIT. The RMS maps created by Drizzle account for the “intrinsic” sources of noise, e.g. dark current, readout noise, and background noise (Koekemoer et al. 2011). The Poisson noise from the sources themselves are readily computed from the images, and are added to the RMS maps in quadrature. Where available, the exposure time maps were used to convert the images, in electrons per second, to electrons for this computation. Otherwise, the median exposure time was used instead.

A “segmentation vector” was then created which, for each pixel, lists the IDs of objects which contribute light

to that pixel. This was done by stacking the Kron ellipses (semi-major axis equal to  $2 \times \text{A\_IMAGE} \times \text{KRON\_RADIUS}$  from SEXTRACTOR) of every object in the image. Ellipses are readily generated from the CXX\_IMAGE, CYY\_IMAGE and CXY\_IMAGE ellipse parameters. Neighbours which overlap with a given object are then the unique set of IDs within this object’s Kron ellipse. For each object, a cutout large enough to contain all overlapping neighbours was created from both the image and the total noise map. Overlapping neighbours are fit simultaneously with the object in question. Bad pixels and non-overlapping neighbours were masked by supplying GALFIT with a mask image where bad pixels and pixels within the Kron ellipses of irrelevant sources were given a value of 1, with all other pixels 0. Finally, a PSF image was created at the object’s position from the PSFEX model.

Absolute magnitudes and physical sizes were computed from the GALFIT model parameters assuming all sources in an image lie at their respective cluster redshifts (Table 1). We circularized the effective radii using  $R_{e,c} = R_e \sqrt{b/a}$ . The mean surface brightness within  $R_e$  was derived from the model magnitudes  $m$  and effective radii using

$$\langle \mu \rangle_e = m + 2.5 \log(2\pi R_{e,c}^2). \quad (1)$$

The absolute mean surface brightness is then calculated with

$$\langle \mu \rangle_{e,abs} = \langle \mu \rangle_e - 2.5 \log(1+z)^4 - E(z) - K(z), \quad (2)$$

where  $z$  is the cluster redshift, and  $E(z)$  and  $K(z)$  are the evolutionary and  $K$ -corrections, respectively (Graham & Driver 2005), computed with EzGal (Mancone, & Gonzalez 2012) assuming a simple stellar population (SSP) with  $[\text{Fe}/\text{H}] = -0.6$ , a formation redshift of  $z = 2$  and a Chabrier (2003) initial mass function.

#### 3.3. Ultra-diffuse galaxy selection

Our UDG selection is very similar to that used in our previous work on Abell 2744 (Janssens et al. 2017), which in turn is based on the cuts used by van der Burg et al. (2016). In this work, instead of transforming all the UDG  $F814W$  surface brightnesses to the  $r$ -band, we instead transform the  $r$ -band surface brightness cut of  $\langle \mu \rangle_{e,abs,r} > 23.8$  mag arcsec $^{-2}$  into a  $F814W$  cut using the same SSP described above for the evolutionary and  $K$ -corrections. The cuts are as follows:

- Circularized half-light radius in the range  $1.5 \text{ kpc} \leq R_{e,c} < 10 \text{ kpc}$ .
- Sérsic index  $n < 4$ . Roughly 97% of injected  $n = 1$  profiles have a recovered  $n < 4$  (see §3.5).
- Absolute mean surface brightness within  $R_e$   $\langle \mu \rangle_{e,abs,F814W} > 24.1$  mag arcsec $^{-2}$ . For radial profiles and estimating the total abundance in each cluster, only UDGs with a mean surface brightness within  $R_e$  brighter than  $\langle \mu \rangle_{e,F814W} = 26.9$  mag arcsec $^{-2}$  are included, this is the 50% completeness limit (see §3.5).
- Axis ratio  $q \equiv b/a > 0.3$ . Coma UDGs are prolate with  $\langle q \rangle \sim 0.7$  (Burkert 2017) and Chen et al. (2010) found no Virgo dwarfs flatter than 0.35.



**Table 1**  
Frontier Fields Cluster Properties and UDG Abundances

Cluster	$z_{cl}$	R.A. <sup>a</sup> (J2000.0)	Dec. <sup>a</sup> (J2000.0)	$M_{200}^b$ ( $10^{15} M_{\odot}$ )	$R_{200}^b$ (Mpc)	Number of UDGs Raw <sup>c</sup>	Total <sup>d</sup>
Abell 2744	0.308	00:14:20.70	−30:24:00.58	$2.06 \pm 0.42$	$2.35 \pm 0.16$	99	$1351^{+387}_{-379}$
Abell S1063 <sup>e</sup>	0.348	22:48:43.97	−44:31:51.14	$1.88 \pm 0.67$	$2.38 \pm 1.48$	167	$1416^{+1877}_{-1127}$
Abell 370	0.375	02:39:52.94	−01:34:37.00	$3.16 \pm 0.38$	$2.66 \pm 0.11$	65	$711^{+213}_{-210}$
MACSJ0416.1−2403	0.396	04:16:08.38	−24:04:20.80	$1.07 \pm 0.26$	$1.88 \pm 0.69$	66	$219^{+230}_{-164}$
MACSJ1149.5+2223	0.543	11:49:35.70	+22:23:54.73	$2.50 \pm 0.54$	$2.35 \pm 1.00$	109	$582^{+397}_{-364}$
MACSJ0717.5+3745	0.545	07:17:32.63	+37:44:59.70	$2.68 \pm 0.55$	$2.36 \pm 0.77$	91	$609^{+438}_{-359}$

<sup>a</sup> Cluster centres were adopted as follows: A2744, location of BCG nearest X-ray centroid; AS1063, location of BCG; A370, midpoint between BCGs (Lagattuta et al. 2017); M0416, midpoint between BCGs (Zitrin et al. 2013); M1149, location of BCG; and M0717, mean location of red sequence members (Medezinski et al. 2013).

<sup>b</sup> Determined from gravitational lensing analyses.  $M_{200}$  and  $R_{200}$  for A2744 are from Medezinski et al. (2016), A370 from Umetsu et al. (2011). Values for the other clusters are from Umetsu et al. (2016).

<sup>c</sup> Total number of UDGs detected in the cluster and parallel fields.

<sup>d</sup> Estimate of the total number of UDGs within  $R_{200}$  after background, completeness and geometrical corrections.

<sup>e</sup> Also known as RXCJ2248.7−4431.

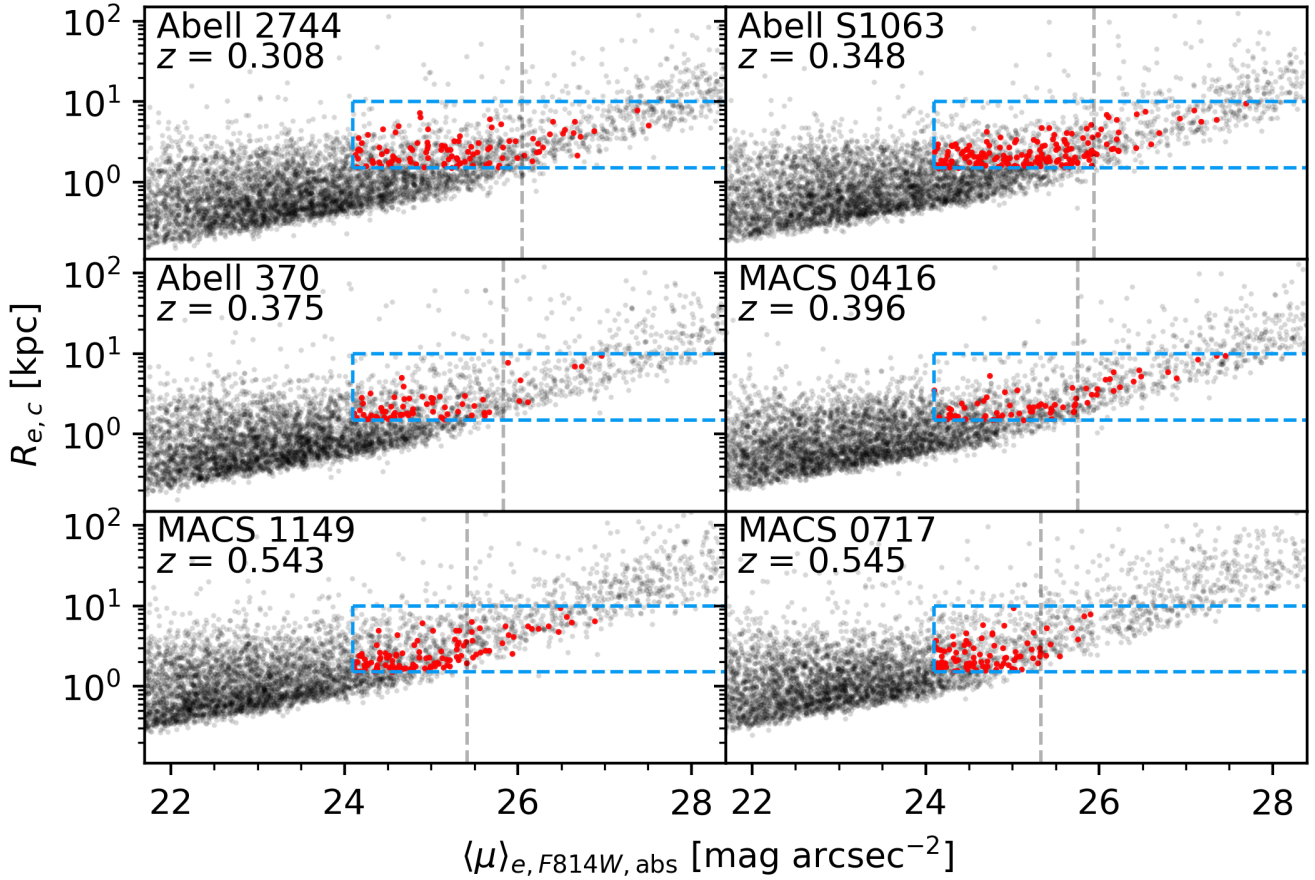


**Figure 1.** UDG selection by size and absolute mean surface brightness within  $R_e$ . Effective radii and absolute surface brightnesses are computed assuming all detected sources reside at the cluster redshift. The UDGs, shown in red, are selected with  $\langle \mu \rangle_{e,abs,F814W} > 24.1 \text{ mag arcsec}^{-2}$  and circularized effective radii in the range  $1.5 \text{ kpc} \leq R_{e,c} < 10 \text{ kpc}$  (blue dashed lines). The additional cuts, including a visual inspection, are described in the text. The dashed vertical grey line corresponds to the 50% mean surface brightness completeness limit of  $26.9 \text{ mag arcsec}^{-2}$ , transformed to the redshift of each cluster.



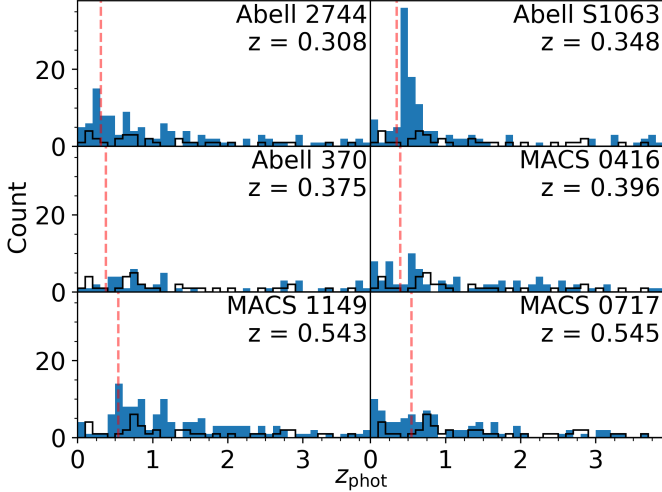


**Figure 2.** The ASTRODEEP photo- $z$  distributions of sources that pass our UDG selection cuts are shown in blue (sources with  $z_{\text{phot}} \geq 1$  were not visually inspected). Objects in the XDF that pass the cuts for each cluster are shown in black. The vertical line is the redshift of the cluster.

This also has the benefit of removing edge-on disks and lensing arcs.

- Photometric redshift  $z_{\text{phot}} < 1$ , if available. Not every UDG candidate has a match in the ASTRODEEP catalogs, but this removes known high- $z$  background objects.
- Within the WFC3/IR footprint for uniform photometric redshift accuracy.

The selection in size and surface brightness parameter space is shown in Figure 1.

Photometric redshifts for all six clusters were obtained from the ASTRODEEP catalogs (Castellano et al. 2016; Merlin et al. 2016; Bradac et al. 2019). We matched our catalog to that of ASTRODEEP by finding the nearest neighbour within  $0.15''$ , or 5 ACS pixels. The distribution of photo- $z$ 's of sources that pass the UDG selection cuts is shown in Figure 2. Photo- $z$ 's were not used in the computation of physical sizes and absolute magnitudes since not every UDG has a match in the ASTRODEEP catalog.

All UDG candidates were visually inspected. Of the 1190 candidates, 636 UDGs were kept. The most common contaminants are deblended objects (i.e. spiral arms, lensing arcs and tidal features split into multiple objects by SEXTRACTOR) and compact ( $n \sim 3.5$ ) galaxies with high central surface brightnesses that do not visually resemble UDGs. Finally, 18 duplicate UDGs were removed where a UDG was deblended into multiple sources, in which case the brighter object was kept. In a few of these cases, SEXTRACTOR picked out an offset overdensity, similar in appearance to DGSAT I (Martínez-Delgado et al. 2016). The raw number of UDGs detected in each cluster is listed in Table 1. Figure 3 shows the locations of all selected UDGs within the WFC3 coverage (pink outline) for each cluster core field, along with  $15 \times 15$  kpc zoom-ins on select UDGs.

Note the remarkable non-uniform projected spatial distributions of UDGs in some of the clusters, most notably

in Abell 2744, MACS 1149 and MACS 0717. Only in Abell S1063 and Abell 370 do the UDGs appear to be evenly distributed around the cluster. In the other clusters, there appear to be many more UDGs on one side than the other. UDGs also appear to avoid the central regions of the clusters. For now though, we turn to corrections and simulations needed to understand the physical significance of these effects, if any.

### 3.4. Background correction

For each FF cluster, an estimate of the background contamination of the UDG sample is made by computing the physical sizes and absolute surface brightness of every XDF source assuming the source lies at the FF cluster redshift. We then apply the UDG cuts described above. By assuming that all XDF sources lie at the FF cluster redshift of  $z = 0.308$ – $0.545$ , the assumed physical scale together with  $(1+z)^4$  cosmological dimming conspire to turn distant high- $z$  galaxies into objects consistent with UDGs. In order to remove these from the background correction count, our XDF catalog was matched to the UVUDF photo- $z$  catalog of Rafelski et al. (2015). The photo- $z$  distributions of XDF sources that pass the UDG cuts in each cluster are shown as the black histograms in Figure 2.

### 3.5. Image simulations

Two sets of image simulations were performed. The first was to determine and inform the selection criteria used to select UDGs, and the second was to determine geometrical completeness distributions of objects that pass our selection criteria in the six clusters.

We began by injecting 2000 simulated objects into each of the cluster and parallel image pairs at random positions in the region with overlapping ACS and WFC3 coverage. The SEXTRACTOR segmentation map was used to ensure that a chosen location was empty. To prevent crowding, this was done in batches of 20, with no pair of injected objects permitted to be closer than 150 pixels. To ensure enough objects were injected at small radii, positions were chosen in radial coordinates for the cluster fields. The simulated objects were single Sérsic profiles generated using GALFIT with the following parameters: Sérsic index  $n = 1$ , circularized effective radius  $1.5 \text{ kpc} \leq R_{e,c} < 10 \text{ kpc}$ , central surface brightness  $17 \text{ mag arcsec}^{-2} < \mu_0 < 29 \text{ mag arcsec}^{-2}$ , axis ratio  $0.3 \leq b/a < 1.0$ , and position angle  $0^\circ \leq \theta < 360^\circ$ . Sets of parameters that resulted in objects much too bright to be a UDG ( $\langle \mu \rangle_{e,\text{abs},F814W} < 23.5 \text{ mag arcsec}^{-2}$ ) or far too faint to be reliably detected ( $m_{F814W} > 28.5$  or  $\langle \mu \rangle_{e,F814W} > 29.5 \text{ mag arcsec}^{-2}$ ) were thrown out and redrawn. The simulated images were then analyzed with the same pipeline described above, with the exception that only the nearest detected object within 5 pixels of an injected location was selected for GALFIT fitting. Roughly 97% of recovered objects have a Sérsic index  $n < 4$ . Figure 4 shows the recovery fraction as a function of effective radius and magnitude. We find a 50% completeness limit of  $\langle \mu \rangle_{e,F814W} = 26.9 \text{ mag arcsec}^{-2}$  with no significant variation between the six clusters.

The geometrical completeness simulations are similar, but we only inject objects that would pass our selection criteria and that are brighter than the 50% completeness

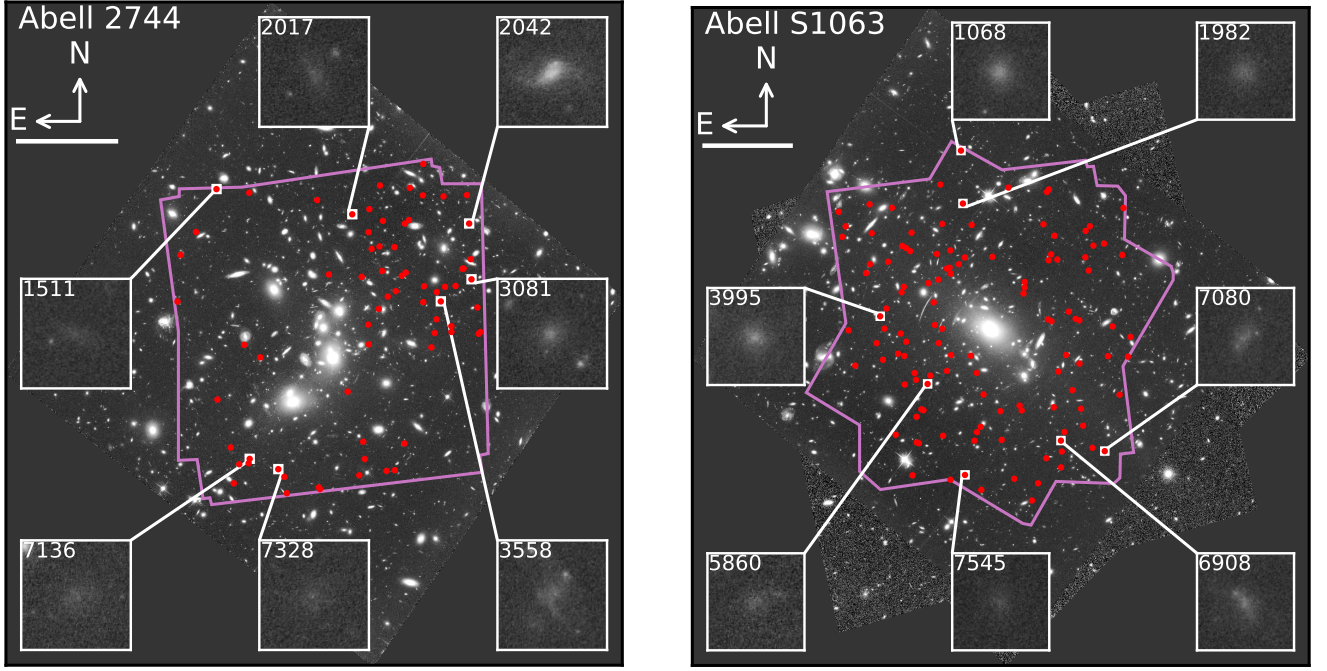


**Figure 3.** Locations of selected UDGs (red points) in the Abell 2744 and Abell S1063 cluster core fields. The background image is the ACS *F814W* image and the pink border is the extent of the WFC3/IR coverage. North is up and east is to the left. The bar below the compass corresponds to 200 kpc. Insets show zoom-ins on select UDGs, the sizes of which are 15 kpc a side.

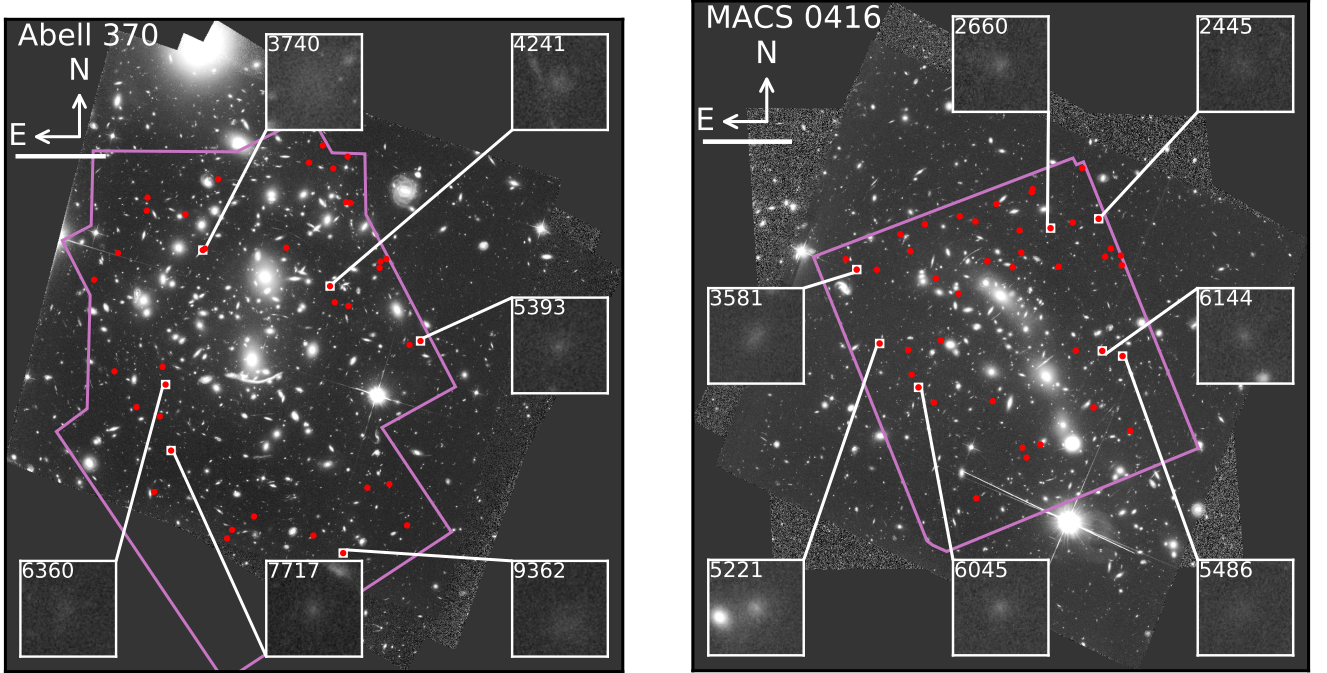


**Figure 3.** (Continued.) Abell 370 and MACS 0416 cluster core fields.

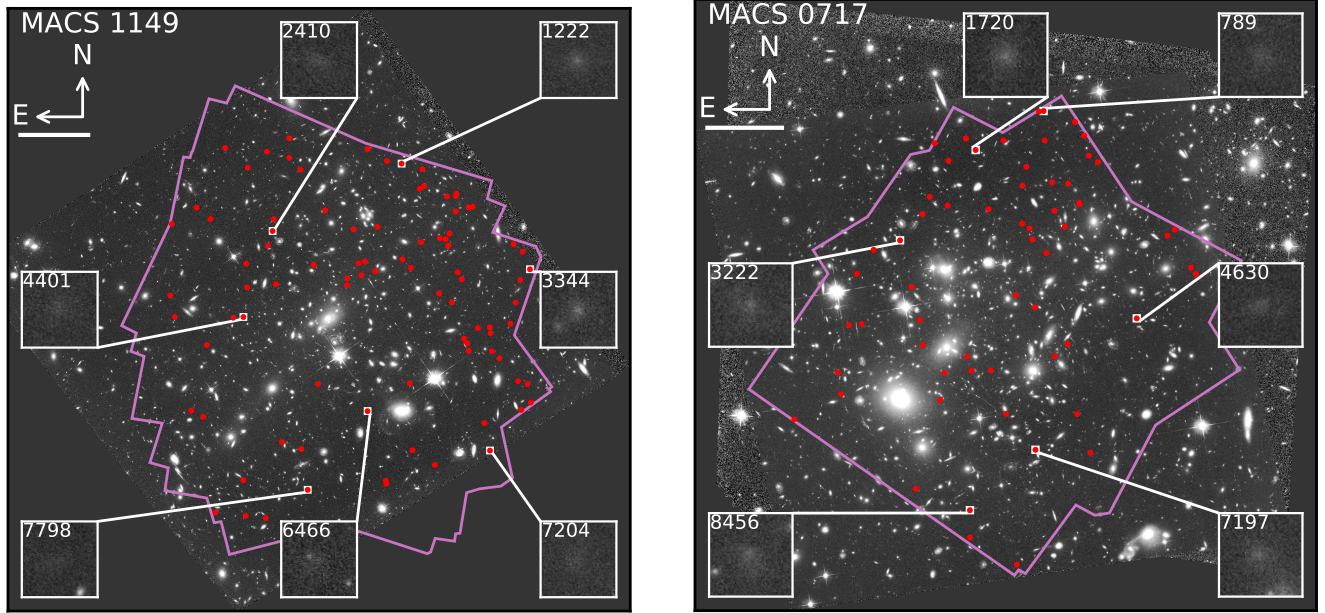


**Figure 3.** (Continued.) MACS 1149 and MACS 0717 cluster core fields.



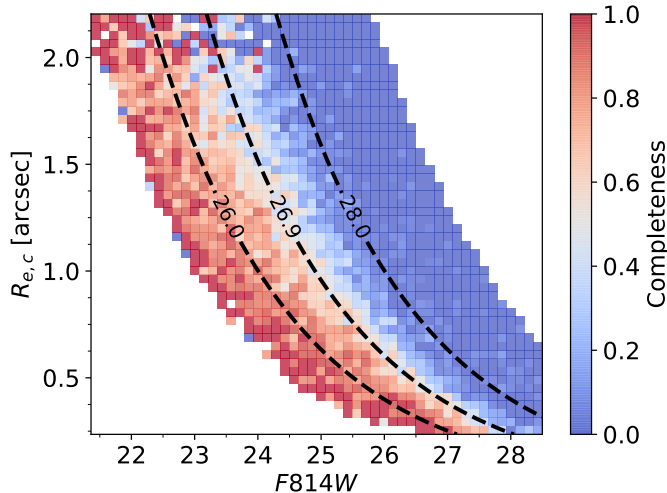


**Figure 4.** Recovery fraction as a function of size and magnitude for  $n = 1$  Sérsic profiles. The lines are contours of mean surface brightness within  $R_e$  ( $\langle \mu \rangle_{e,F814W}$ ) in units of  $\text{mag arcsec}^{-2}$ ; 26.9  $\text{mag arcsec}^{-2}$  is the 50% completeness limit.

limit found above. We allow any location in the ACS and WFC3 overlap region to be chosen, informing the fraction of UDGs that may be lost due to projection against other sources or the intracluster light (ICL). The minimum spacing of 150 pixels between injected objects is still enforced. The resulting radial completeness curves are shown in the right-hand panels of Figure 6, the rest of the figure is discussed later in the context of the radial density profiles of UDGs.

### 3.6. Ultra-compact dwarf selection

UDGs were selected from a separate catalog optimized for point source detection since even the largest UDGs ( $r_h \sim 100$  pc, Brodie et al. 2011) would be unresolved in the lowest redshift FF cluster. A median filter with a kernel size of 15 pixels was applied to the  $F814W$  image of each field and subtracted off to remove low frequency power from the BCGs and the ICL. The resulting image was then used by SExtractor as the detection image in dual-image mode for all bands, with measurements performed on the unfiltered images. Magnitudes were measured in 4 pixel diameter apertures. Aperture corrections were applied by first correcting to a  $1''$  diameter (33.3 pixels) aperture and then Table 5 in Sirianni et al. (2005) was used to correct from the  $1''$  aperture to infinity. Since the PSF varies spatially across each image, the PSFEX model was used to compute the correction to a  $1''$  aperture at the location of every detected source.

Point sources were selected from this catalog on the basis of shape, requiring  $e \equiv 1 - b/a < 0.4$ , size, requiring  $\text{FLUX\_RADIUS} < 10$  pixels, and image concentration, requiring  $0.8 < C_{3-7} < 1.2$ , where  $C_{3-7}$  is the difference between an object’s magnitude measured in a 3 and 7 pixel diameter aperture. The  $F606W, F814W$  colour-magnitude diagrams (CMDs) for point sources in the FFs are shown in Figure 5. Since UDGs are expected to be found in the densest environments (Pfeffer & Baumgardt 2013), we select UDGs in only the cluster fields and use the parallel fields to estimate the contamination from unresolved galaxies and foreground stars. The boxes shown in Figure 5 are the UCD se-

lection regions which are the apparent  $F814W$  magnitudes and  $F606W - F814W$  colours spanned by SSPs with formation redshifts  $2 < z < 10$  and metallicities  $-2.25 < [\text{Fe}/\text{H}] < -0.33$  at the redshift of each cluster. The bright magnitude limit corresponds to a mass of  $10^7 M_\odot$  and the faint limit is the 50% completeness limiting magnitude for the cluster field determined using artificial star tests (see Appendix B). The limiting magnitudes are well above the magnitudes of the most massive GCs, with GCs expected to have apparent magnitudes  $m_{814} \gtrsim 31$  mag. The number of sources that reside within the selection box is listed for each field in Figure 5. An excess of UCD candidates in the cluster core field is observed for all clusters, with the exception of MACS 1149.

In the Abell 370 cluster core field CMD, the sequence of sources bluer than the UCD selection box at  $F606W - F814W \sim 0.5$  are likely GCs associated with the foreground elliptical galaxy PGC 175370 at a distance of  $\sim 200$  Mpc. This is the galaxy on the northern edge of the ACS field in Figure 3. Photometric scatter at the faint end is a source of foreground contamination not captured by the parallel field. Restricting the UCD analysis to the region with WFC3 coverage removes the most likely contaminants (see Figure 14).

## 4. RESULTS AND DISCUSSION

### 4.1. Radial distributions

Radial profiles of the surface density of UDGs were made for each of the six clusters and are shown in Figure 6. The location of the BCG was adopted as the cluster centre, or in the case of multiple BCGs, their midpoint; these are listed in Table 1. For each cluster, the leftmost panels in Figure 6 show the raw observed radial densities (black points) along with the density of background sources estimated from the number of XDF sources that satisfy each cluster’s UDG cut (gray dotted line, roughly  $\sim 2 \text{ arcmin}^{-2}$ ). The central panels shows the profile after correcting for the completeness in each radial bin (right panels) and subtracting off the background density. In all six clusters, either a central depletion or a flattening out of the radial profile of UDGs is observed. This behaviour has been described in several nearby clusters (e.g. van der Burg et al. 2016; Mancera Piña et al. 2018) and is thought to be caused by the tidal disruption of UDGs near the centres of galaxy clusters. However, using simulations, Sales et al. (2019) find that the surface density of UDGs rises continually towards the centre of a Virgo-like cluster. At radii inside  $\sim 0.4 \times R_{200}$ , “tidal UDGs”, a population of galaxies transformed into UDGs as a result of tidal stripping, begin to dominate the population, as UDGs that fell into the cluster as UDGs are now destroyed. Finally, it should also be noted that the highly disturbed nature of the FF clusters renders the choice of cluster centre rather uncertain.

### 4.2. The abundance of ultra-diffuse galaxies

An estimate for the total number of UDGs in each cluster is made by integrating the corrected surface number density profile out to  $R_{200}$ . These total abundances are listed in the last column of Table 1 and range from  $\sim 200$  in MACS 0416 to  $\sim 1400$  in Abell 2744 and Abell S1063. Note that for Abell 2744, Abell S1063 and Abell 370,

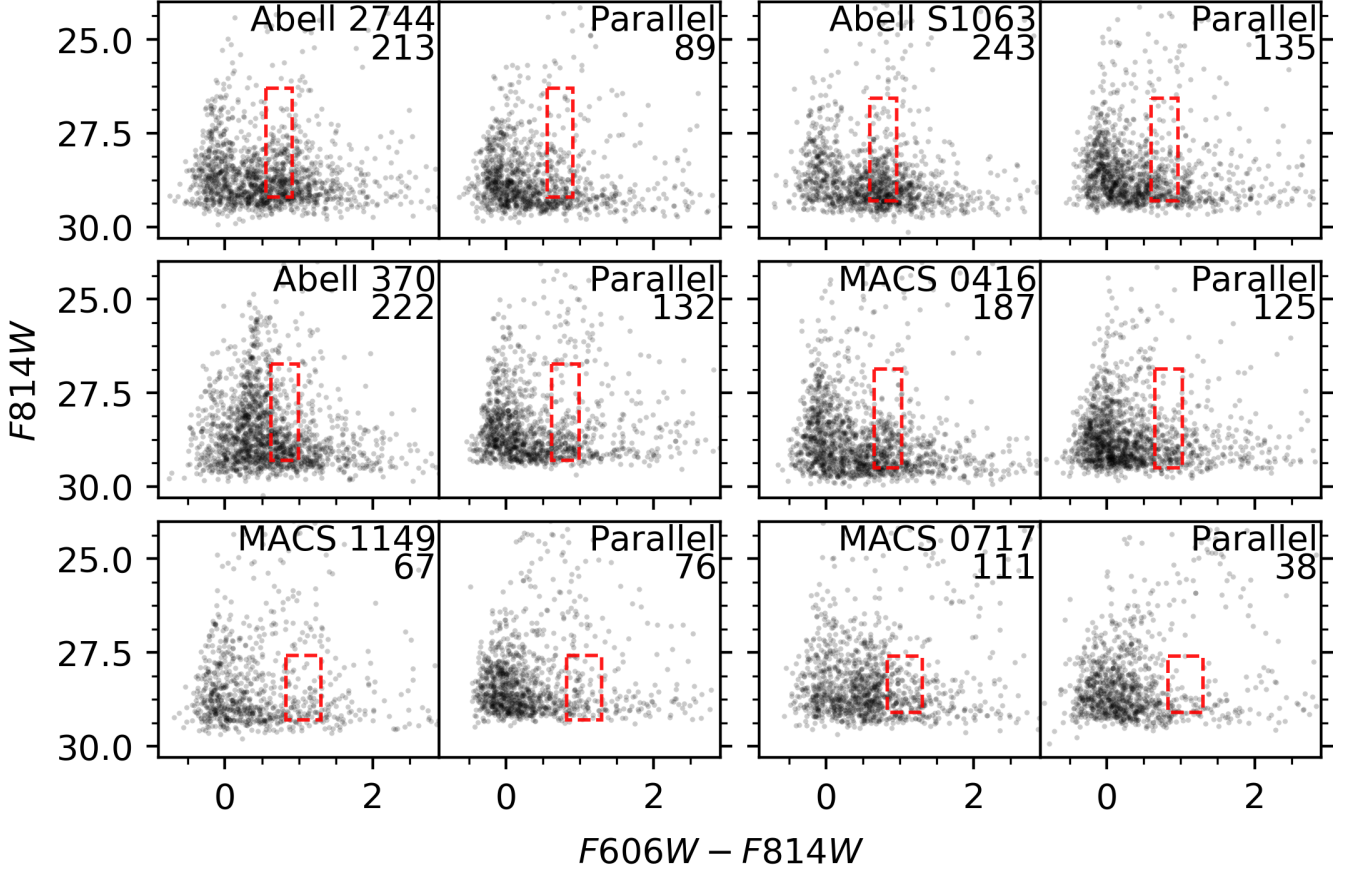


**Figure 5.** Colour-magnitude diagrams for unresolved sources in each of the cluster (left panels) and parallel (right) fields. The boxes are the UCD selection regions, described in the text. The numbers in the top right are the total number of UCD candidates in each field. UCDs are expected to be found in the densest regions so the parallel fields are used to estimate the contamination from unresolved galaxies and foreground Milky Way stars.

where we have to extrapolate out to  $R_{200}$ , we assume the surface density observed in the parallel field is constant out to  $R_{200}$ . The upper and lower estimates were obtained by integrating along the lower and upper error bars of the corrected profile, out to the upper and lower bounds of  $R_{200}$ , respectively. The large range in the abundance of UDGs in Abell S1063 is a result of its  $R_{200}$  value being poorly constrained.

Our new estimate for the abundance of UDGs in Abell 2744 of  $1351^{+387}_{-379}$  is slightly lower than, but consistent with, our previous result of  $1961 \pm 577$  (Janssens et al. 2017). This is due to our revised UDG selection, most notably that UDGs in Abell 2744 fainter than the 50% completeness limit of  $\langle \mu \rangle_{e,F814W} = 26.9$  mag arcsec $^{-2}$  were excluded from the estimate in this analysis. The mass of Abell 2744 has been slightly lowered in this analysis as well. In Janssens et al. (2017), an ensemble mass estimate from lensing and dynamical studies was used, but here we only use a lensing mass estimate to be consistent with the other five clusters studied.

In Figure 7, we update the UDG abundance halo-mass relation including all six FF clusters, along with the abundances in other systems from the literature. van der Burg et al. (2016) investigated the UDG populations in eight clusters at redshifts  $0.044 < z < 0.063$ . van der Burg et al. (2017) extended this investigation to lower

masses, looking at 325 galaxy groups from the GAMA survey in seven mass bins. For Coma, we apply our UDG criteria to the Yagi et al. (2016) catalog finding  $\sim 200$  such objects. And similarly for Fornax, we apply our selection criteria to the Muñoz et al. (2015) catalog. This catalog, however, only covers the inner 350 kpc so we apply a geometrical correction by assuming the flat radial surface density profile they found for dwarfs applies to UDGs out to  $R_{200} = 700$  kpc (Drinkwater et al. 2001) and we estimate a total of  $\sim 30$  UDGs. Finally, we include the abundances of UDGs in Abell 168 and UDG 842 (Román, & Trujillo 2017a) and three Hickson Compact Groups (Román, & Trujillo 2017b).

In the Virgo cluster, Impey et al. (1988) identify 27 large low surface brightness galaxies. Most have scale lengths  $h \gtrsim 10''$  and central surface brightnesses in the  $B$ -band fainter than  $\mu_{0,B} \approx 23$  mag arcsec $^{-2}$ . For  $n = 1$  Sérsic profiles,  $\langle \mu \rangle_e = \mu_0 + 1.12$  and the effective radius is related to the scale length via  $R_e = 1.678h$  (Graham & Driver 2005), meaning they have  $R_e \gtrsim 1.5$  kpc $^6$  and  $\langle \mu \rangle_{e,B} \gtrsim 24$  mag arcsec $^{-2}$ , satisfying the rough definition of a UDG. In their Figure 7b, we find a total of 37 galaxies that satisfy these cuts, including an additional 19 objects they include from Caldwell (1983).

<sup>6</sup> Adopting a distance of 16 Mpc to the Virgo cluster.

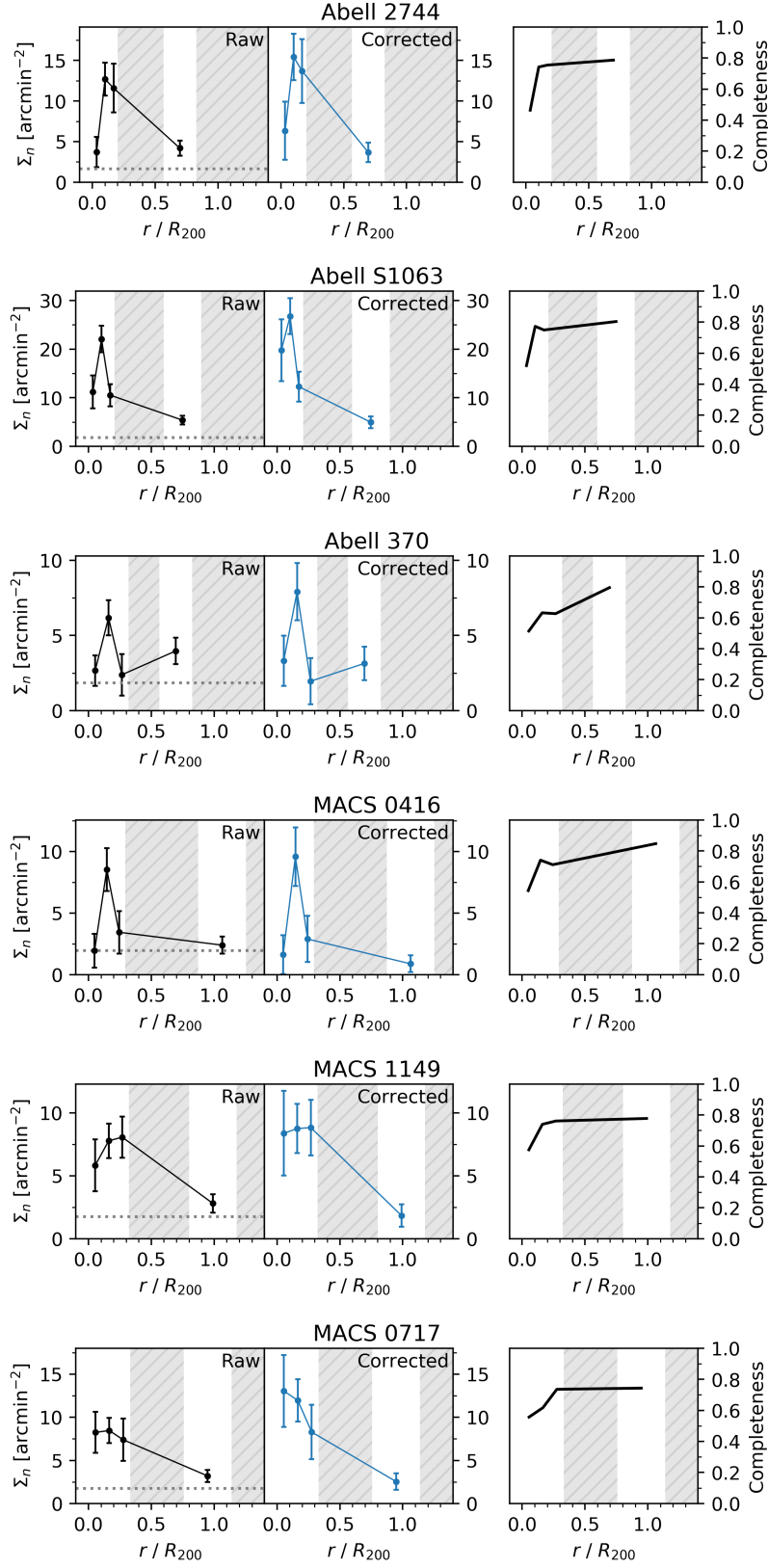


**Figure 6.** Radial surface number density profiles of UDGs in the six FF clusters. For each cluster, the points in the leftmost panels are the raw observed surface densities and the dotted line is the density of background sources estimated from the XDF. The rightmost panels shows the completeness fractions in each bin determined from our image simulations (see text for details). The middle panels show the radial profiles after correcting for completeness and subtracting off the estimated background contamination. The hatched shaded regions denote radii with no coverage (e.g. between the cluster and parallel fields).



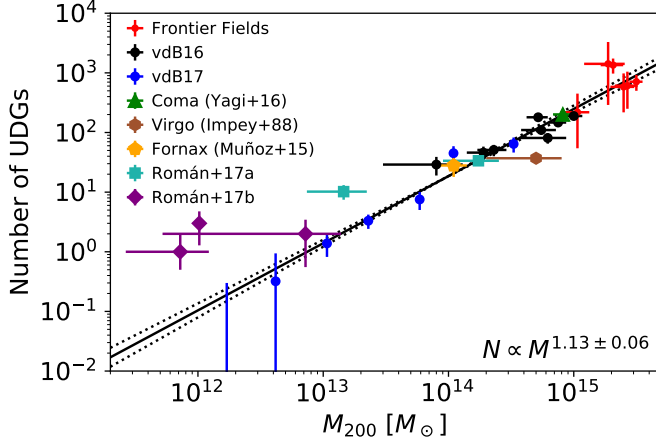


**Figure 7.** Abundance of UDGs as a function of halo mass for the six FF clusters examined in this work, as well as other systems from the literature (see text for details). The solid line is the best fit power law to the abundances in the FFs as well as the binned groups from [van der Burg et al. \(2017\)](#) and the clusters from [van der Burg et al. \(2016\)](#).

[van der Burg et al. \(2017\)](#) fit a power law to the UDG abundance halo-mass relation and found  $N_{\text{UDG}} \propto M_{200}^{1.11 \pm 0.07}$  using the abundances in 325 galaxy groups at  $0.01 \leq z \leq 0.10$  in seven mass bins and the abundances in eight clusters at redshifts  $0.044 < z < 0.063$  from [van der Burg et al. \(2016\)](#). The six FF clusters are  $\sim 0.5$  dex higher in mass than the most massive system investigated in [van der Burg et al. \(2016\)](#). To see what effect these massive systems have on the abundance halo-mass relation, we reperformed the fit including these new clusters. Orthogonal distance regression was used to fit the power law, allowing the fit to account for uncertainty in both  $N_{\text{UDG}}$  and  $M_{200}$ . We find a best fit relation of

$$N_{\text{UDG}} = (19 \pm 2) \left[ \frac{M_{200}}{10^{14} M_{\odot}} \right]^{1.13 \pm 0.06}, \quad (3)$$

showing that the abundance of UDGs in these extremely massive systems at intermediate redshift is in excellent agreement with the relation from [van der Burg et al. \(2017\)](#) describing more local and less massive clusters.

The slope of this relation is interesting for its implications regarding the environments where UDGs may be preferentially created or destroyed. A slope of unity means that as structures hierarchically merge, the number of UDGs is conserved. A slope less than one would suggest that UDGs are more easily created in group environments, or that they may be preferentially destroyed in clusters ([Román, & Trujillo 2017b](#)). On the other hand, a slope greater than unity, as we find, suggests that the group environment is destructive to UDGs, or that there is a process that can preferentially create UDGs in cluster environments ([Román, & Trujillo 2017b](#); [van der Burg et al. 2017](#)), with tides having already been discussed as one possibility ([Sales et al. 2019](#)).

The morphology of galaxies residing in clusters changes dramatically between  $z \sim 0.4$  and  $z = 0$  (i.e. the Butcher-Oemler effect, [Butcher, & Oemler 1978, 1984](#); [Dressler et al. 1994](#); [Moore et al. 1998](#)). The amount of light in the ICL has also grown by a factor of 2–4 since  $z \sim 1$  ([Burke et al. 2012](#)), and the tidal disruption of galaxies is understood to be its origin (e.g. [Harris et al. 2017](#)). This

suggests there is a big caveat to including the abundances of UDGs in both local and intermediate redshift systems on the same abundance halo-mass relation as it is not unreasonable to believe that this relation has evolved since  $z \sim 0.4$ , with these processes destroying (or creating) UDGs as clusters have continued to assemble over the past  $\sim 4$  Gyr. That said, the abundance of UDGs in these extremely massive intermediate redshift clusters agrees very well with the relation at  $z \sim 0$ .

#### 4.3. Spatial distributions

We now return to the remarkable projected spatial distributions of UDGs that we first drew attention to in §3.3. Maps were made to investigate the spatial distributions of UDGs and UCDs and their relation to other structures in the clusters. These are shown in Figure 8. We restrict ourselves to the WFC3 region (pink outline) as this is where our UDG selection was performed. The red points are the locations of UDGs while UCDs are marked in black. The blue triangles mark the positions of other cluster galaxies, selected with  $R_{e,c} \geq 0.5$  kpc and  $|z_{\text{phot}} - z_{\text{cl}}| \leq 0.05$ , where  $z_{\text{cl}}$  is the cluster redshift. Black text labels mark the positions of mass peaks from gravitational lensing analyses in the literature, which we include to see whether there is any possible relationship between substructures and concentrations of UDGs. The red-yellow contours are smoothed *Chandra* X-ray fluxes (ObsIDs 8477, 18611, 515, 16304, 16306 and 16305) tracing the hot intracluster medium (ICM). The blue-green contours are mass surface density contours from the Merten gravitational lensing models<sup>7</sup> ([Merten et al. 2009, 2011](#); [Zitrin et al. 2009, 2013](#)). The X’s mark different possible definitions of the cluster centres: in blue is the peak mass surface density, in pink is the BCG centre (Table 1) and in red is the centroid of the UDG distribution. Multi-lobed mass distributions and/or any disagreement between the mass contours, ICM contours, and the BCGs point towards clusters still in the process of being assembled.

In four of the six clusters, the spatial distribution of UDGs does not appear uniform, with many more UDGs on one side than the other. Only Abell S1063 and Abell 370 present with what appears to be an azimuthally even distribution of UDGs around the cluster. Given the highly disturbed nature of these clusters, this may be expected. However, this behaviour is not seen amongst the other cluster galaxies. We are now in a position to try and understand if this effect is real.

A simple measure of this lopsidedness was devised by finding the line that bisects the cluster which results in the most UDGs being on one side. This line is shown in the top panels of Figure 9, with the positions of UDGs also marked. We also wanted to test whether the uneven distributions were simply a reflection of the completeness fraction across the clusters. To this end, the WFC3 regions of each cluster were split into cells and the completeness fraction was computed in each using our image simulations; this is shown as the background of the top panels of Figure 9. A rough estimate of the completeness corrected number of UDGs,  $N_{\text{cor}}$ , was made by dividing the number of UDGs in each cell by the cell’s complete-

<sup>7</sup> Obtained from <http://www.stsci.edu/hst/campaigns/frontier-fields/Lensing-Models>.

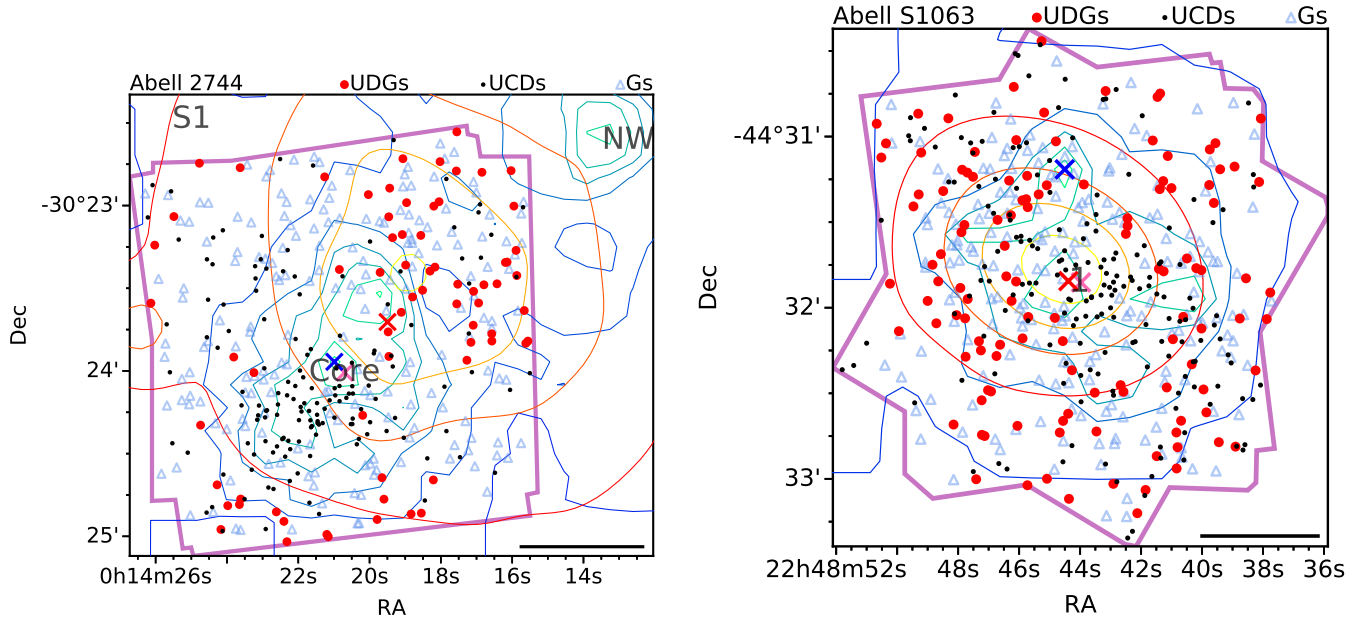


**Figure 8.** Maps showing the projected spatial distributions of various components of the clusters Abell 2744 and Abell S1063 within the WFC3 cluster fields (pink border). The black line in the lower right measures 200 kpc in length. Locations of UCDs are marked in black, UDGs in red, and other cluster galaxies (labelled Gs) are marked in blue. The X's mark different possible adoptions of the cluster centre: pink, the BCG centre (that listed in Table 1); blue, the gravitational lensing mass surface density peak; and red, the mean UDG location. The blue-green contours trace the gravitational lensing surface mass density of the cluster (Merten et al. 2009, 2011; Zitrin et al. 2009, 2013), while the red-yellow contours are Chandra X-ray fluxes. Labels in black correspond to cluster substructures from the literature. In Abell 2744, ‘Core’, ‘NW’ and ‘S1’ are the three substructures identified by Jauzac et al. (2016) that are in proximity to the WFC3 field. The single cluster-scale mass component coincident with the BCG found by Richard et al. (2014) is marked ‘1’ in Abell S1063. UDGs appear deficient in the most dense cluster environments, with UCDs instead being abundant towards the cluster centres. No relationship between UDG locations and the X-ray flux (tracing the hot ICM) is observed, as is expected if UDGs are gas poor systems.

ness fraction and summing. We then performed 1000 simulations of a uniform spatial distribution of UDGs by randomly drawing  $N_{\text{cor}}$  positions and then simulating the completeness by giving each position a probability of being kept equal to the completeness in its cell. The results of these simulations are shown in the bottom panels of Figure 9. Defining lopsidedness as the difference between the more and less populated sides, the histogram shows the distribution of lopsidedness from the simulations and the dashed blue vertical line is the observed value. All but Abell S1063 show spatial distributions of UDGs inconsistent with that expected from a uniform distribution based on our simulations. In the case of Abell 370, the detected UDGs are quite evenly distributed on either side, but based on the completeness, this should not be the case. If the true UDG distribution were uniform, we would expect to detect  $\sim 15$ – $25$  more UDGs in the southern half of the image.

We then performed the same test on the UDGs in the parallel fields. These are shown in Appendix A and Figure 11. In the parallel fields, the distribution appears much more uniform and only one field, the Abell 370 parallel field, shows any evidence of a possible lopsided UDG distribution in the simulations.

We now briefly discuss each of the clusters in turn.

*Abell 2744*— Abell 2744 is a massive complex merging cluster with past and ongoing mergers between at least four substructures (Owers et al. 2011; Merten et al. 2011; Medezinski et al. 2016) and as many as eight (Jauzac et al. 2016). The bulk of the UDGs are located in the northwest quadrant of the field, northwest of the

cluster core. This cloud of UDGs is located roughly midway between the cluster core and a relatively massive NW substructure consistently found in all analyses located  $\sim 580$  kpc northwest of the cluster centre (Merten et al. 2011; Medezinski et al. 2016; Jauzac et al. 2016). Three of the eight substructures identified by Jauzac et al. (2016) that are in proximity to the WFC3 field, including the core and NW substructures, are marked in Figure 8. X-ray observations of the NW substructure reveal a trail of cool gas to the south and a cold front to the north, suggesting this substructure is moving northward on its first infall (Jauzac et al. 2016). The other merger of possible relevance to our UDGs has already occurred and was the passage of the Northern substructure through the cluster core (Owers et al. 2011; Merten et al. 2011; Medezinski et al. 2016). It is possible this collection of UDGs was deposited here in the process of the past north-south merger, or alternatively they are possibly associated with the NW subcluster on its first infall. The UCDs in this cluster are heavily concentrated around the three BCGs southeast of the core mass peak.

*Abell S1063*— Abell S1063 possesses one of the highest known X-ray temperatures and is possibly undergoing a major merger, with the merger axis in the plane of the sky (Gómez et al. 2012). But despite this possible merger, Abell S1063 is the most relaxed FF cluster (Lotz et al. 2017), with the smoothest mass contours (Gruen et al. 2013; Diego et al. 2016). In contrast to the other FF clusters, Richard et al. (2014) only require a single cluster-scale dark matter component to fit the observed lensed images in Abell S1063; the centre of this ‘DM1’

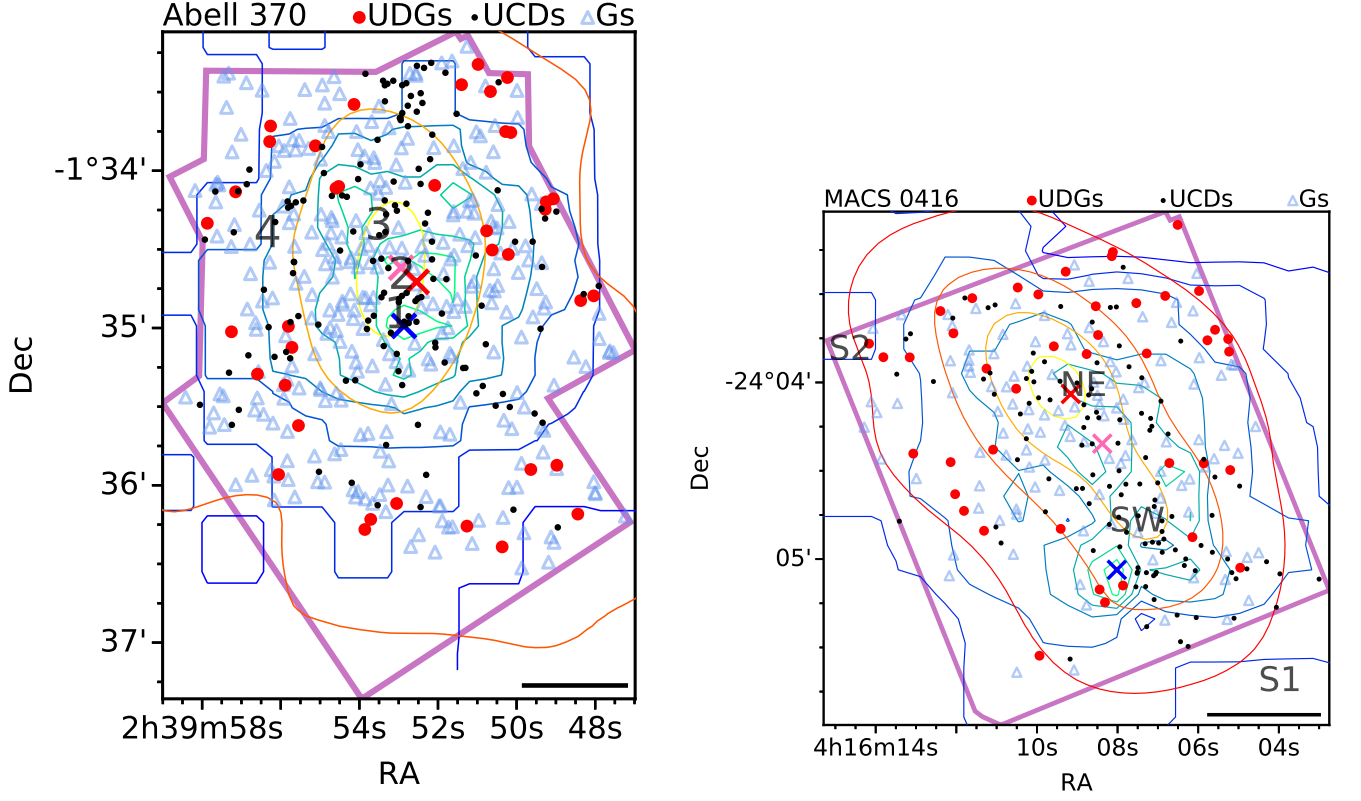


**Figure 8.** (Continued.) Abell 370 and MACS 0416. In Abell 370, 1–4 mark the positions of DM1–DM4, the four ‘large-scale’ mass components identified by [Lagattuta et al. \(2019\)](#). In MACS 0416, NE and SW mark the positions of the two main dark matter halos comprising the core of MACS 0416, while S1 and S2 are two additional galaxy group sized ( $\sim 10^{13} M_{\odot}$ ) substructures, all from [Jauzac et al. \(2015\)](#).

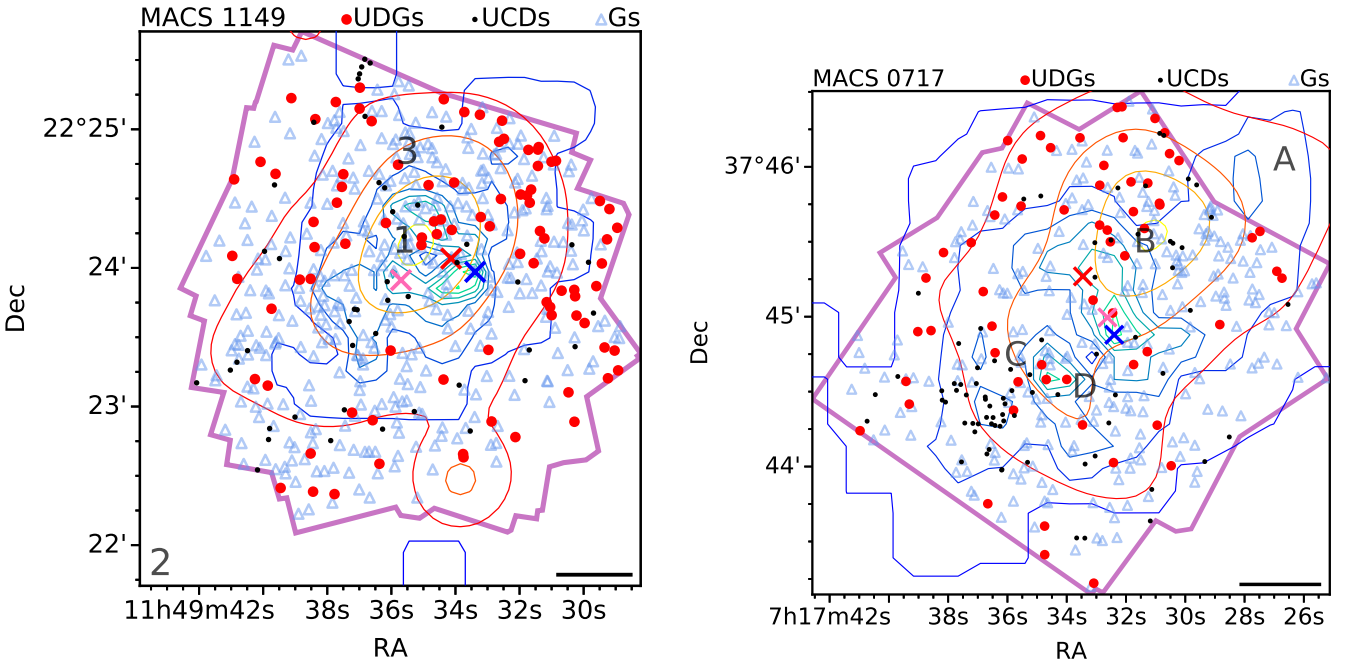


**Figure 8.** (Continued.) MACS 1149 and MACS 0717. In MACS 1149, the positions of the three subclusters identified by [Golovich et al. \(2016\)](#) are marked 1, 2 and 3. In MACS 0717, A, B, C and D mark the [Limousin et al. \(2016\)](#) NFW fit positions of the [Ma et al. \(2009\)](#) light peaks in the cluster core.



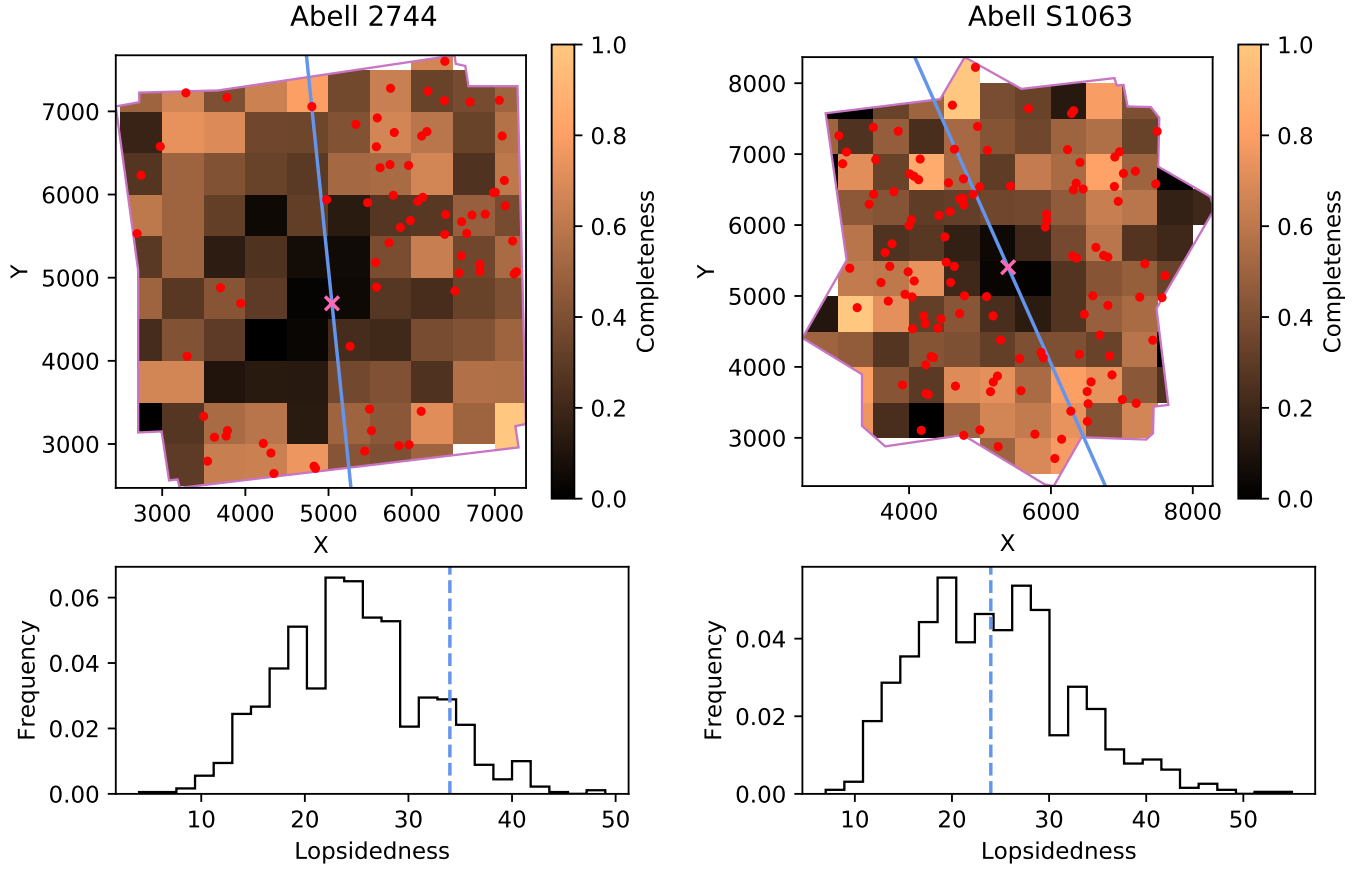


**Figure 9.** A simple test for a lopsided projected spatial distribution of UDGs in the cluster core fields. Top: We search for the straight line that passes through the adopted cluster centre (pink cross, see Table 1) which results in the most UDGs (red points) being on one side. The ACS/WFC3 overlap region is divided into 500 pixel  $\times$  500 pixel cells and the image simulations are used to determine a completeness fraction in each. The pink border is the WFC3  $F160W$  footprint. Blank regions inside the WFC3 footprint are either small slices of cells that had no injected sources in the image simulations or are regions where the WFC3 footprint extends beyond the ACS coverage. Bottom: To test whether this is a real phenomenon or a completeness artifact, for each cluster, we create 1000 realizations of a uniform spatial distribution of UDGs. An estimate of the completeness corrected total number of UDGs,  $N_{\text{cor}}$ , in the core field is made by dividing the number of UDGs in each cell by its completeness fraction.  $N_{\text{cor}}$  locations are then randomly drawn, with each location having a probability of being kept equal to the completeness in that cell. We again search for the line passing through the centre that results in the most lopsided configuration. The distribution of resulting lopsidedness (defined as the difference between the more and less populated sides) is shown, with the observed lopsidedness denoted with the dashed line. This phenomenon is least pronounced in Abell S1063, and this is the most relaxed FF cluster (Lotz et al. 2017).

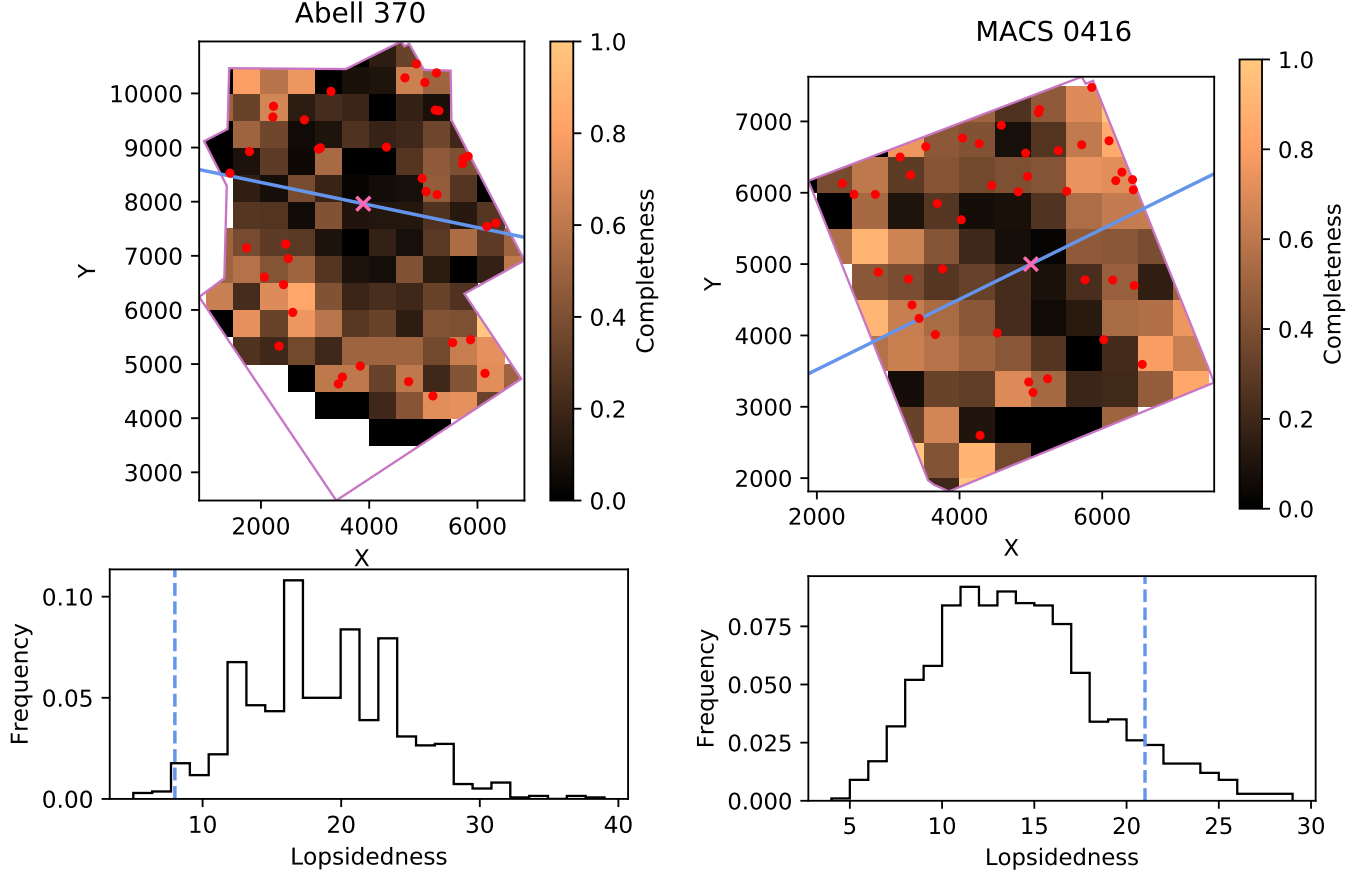


**Figure 9.** (Continued.)

component is coincident with the BCG and is marked ‘1’ in Figure 8. However, in addition to this central halo, [Johnson et al. \(2014\)](#) find two other cluster-scale halos, one  $\sim 400''$  (2 Mpc) to the northeast, and the other  $\sim 100''$  (500 kpc) to the south, but both are well outside the *HST* field of view. Abell S1063 presents the most uniform distribution of UDGs azimuthally around its centre, with the central region deficient in UDGs but abundant in UCDs.

*Abell 370*— Abell 370 is a massive merger of two roughly equal subclusters along the line of sight, with each BCG belonging to one of the subclusters ([Richard et al. 2010](#)). However, while the northern BCG has a slightly higher redshift than its southern counterpart, [Lagattuta et al. \(2019\)](#) find only a single peak in the redshift distribution of the cluster members, suggesting that the merger is either in the plane of the sky or has already taken place. In their best-fit ‘copper-class’ model, [Lagattuta et al. \(2019\)](#) identify four large-scale massive components (DM1–DM4), whose positions are marked 1–4 in Figure 8, in addition to a handful of smaller galaxy-scale components. DM1 and DM3 correspond to the mass clumps associated with the southern and northern BCGs, respectively. DM2 is a ‘bar’ between the two BCGs, and DM4 is associated with a ‘crown’ of galaxies in the northern portion of the field. As discussed above, based on the completeness, the northern region of the Abell 370 WFC3 field is overabundant in UDGs. The UCDs are fairly evenly spread amongst the cluster ellipticals.

There is also the presence of the bright foreground elliptical galaxy PGC 175370 (distance  $\sim 200$  Mpc) on the northern edge of the ACS image to consider (see Figure 3). It cannot be ruled out that some of the ‘extra’ UDGs found in the northern portion of Abell 370 based on our completeness simulations may instead be ‘regular’ dwarf galaxies associated with PGC 175370. The group of UCD candidates at the northern edge of the WFC3 coverage are coincident with a cluster elliptical (compare with Figures 3 and 14). On this basis we believe them to be genuine UCD candidates and not GCs associated with PGC 175370.

*MACS 0416*— MACS 0416 is composed of two main subclusters undergoing a merger. Originally thought to be observed after a possible binary head-on merger ([Mann, & Ebeling 2012](#); [Jauzac et al. 2015](#)), more recent radio and X-ray observations point toward the subclusters in MACS 0416 being observed in a pre-collisional state ([Ogrea et al. 2015](#); [Balestra et al. 2016](#)). Each of the subclusters, however, may have been formed in a recent merger of their own ([Balestra et al. 2016](#)). In Figure 8, we mark the positions of the NE and SW subclusters from [Jauzac et al. \(2015\)](#)<sup>8</sup>, in addition to two galaxy group sized ( $\sim 10^{13} M_{\odot}$ ) substructures they found near the core, S1 and S2. The motion of the SW subcluster is towards us whereas the NE component is receding.

<sup>8</sup> The NE and SW subclusters are denoted C1 and C2 in Table 2 of [Jauzac et al. \(2015\)](#), respectively.

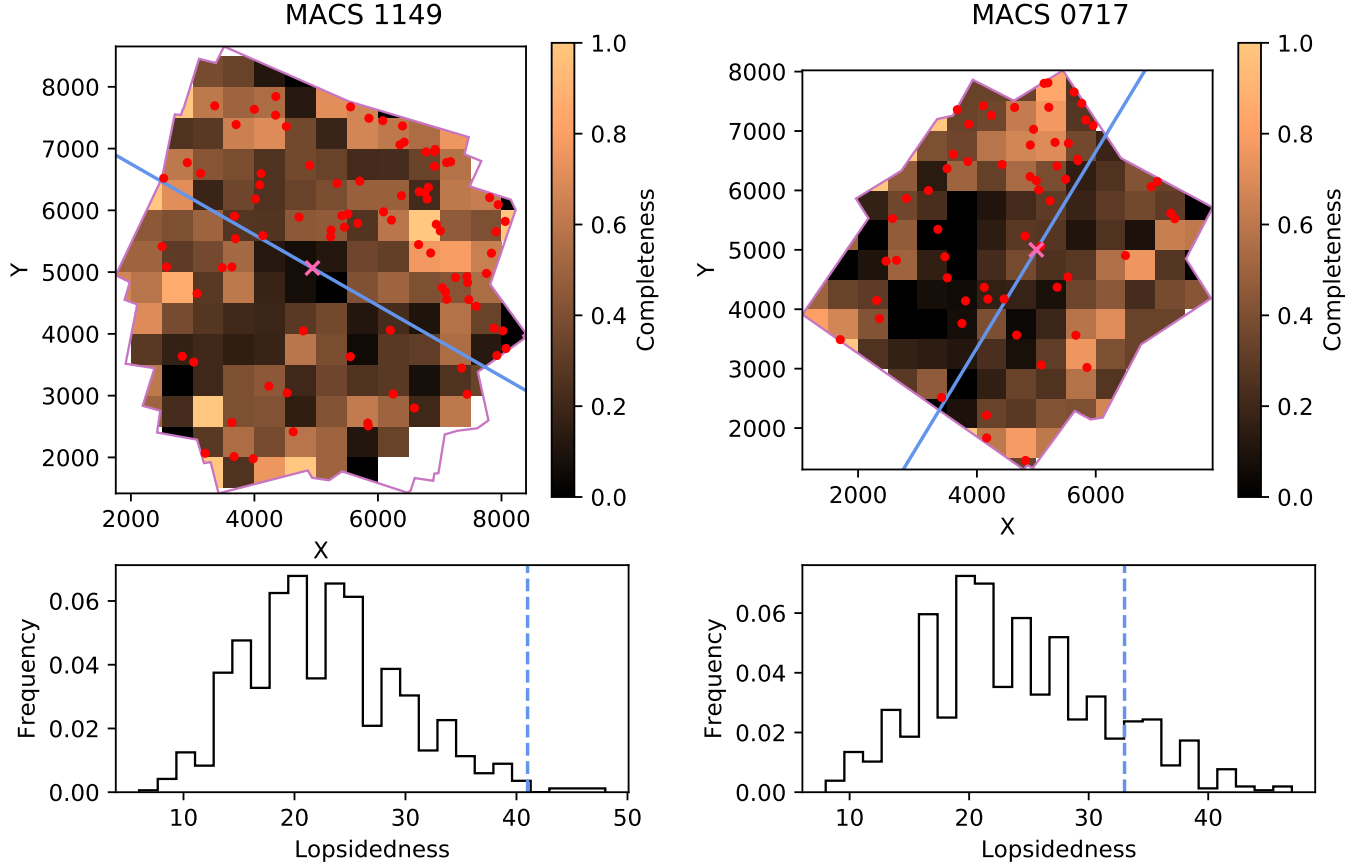


**Figure 9.** (Continued.)

We detect many more UDGs around the NE subcluster than the SW, and a few in the northeast corner may be associated with the S2 substructure. The UCDs in MACS 0416 are concentrated along the bridge of cluster ellipticals and ICL joining the two subclusters.

*MACS 1149*— [Golovich et al. \(2016\)](#) identify three subclusters comprising the core of MACS 1149 and their positions are marked in Figure 8. In their merger scenario, subclusters 1 and 2, with masses of  $\sim 1.7$  and  $\sim 1.1 \times 10^{15} M_{\odot}$ , respectively, have already merged and passed through one another along a merger axis close to the plane of the sky. Subcluster 3 is an order of magnitude less massive with a mass of  $\sim 1.2 \times 10^{14} M_{\odot}$ . Its merger with subcluster 1 is along the line of sight and has recently taken place with the subclusters near pericentre, and subcluster 3 now receding into the background. Interestingly, no concentration of UCDs is seen near the BCG, and there is not an excess of UCD candidates in the cluster field relative to the parallel field. MACS 1149 has the faintest BCG and the least ICL, perhaps hinting that the processes that build these components in clusters are linked to the formation of UCDs.

*MACS 0717*— MACS 0717 is another complex merging cluster. At  $z = 0.545$ , it is the most massive cluster known at  $z > 0.5$  ([Edge et al. 2003](#); [Ebeling et al. 2004, 2007](#); [Jauzac et al. 2018](#)). Its core contains four massive merging components ([Ma et al. 2009](#); [Limousin et al. 2012](#)), surrounded by seven more substructures at

projected radii between 1.6 and 4.9 Mpc ([Jauzac et al. 2018](#)). It also hosts a filament extending a projected distance of  $\sim 4.5$  Mpc to the southeast, with a true length of  $\sim 18$  Mpc, feeding mass into the cluster core from behind ([Ebeling et al. 2004](#); [Jauzac et al. 2012](#)). By  $z = 0.308$ , it will likely be more massive than Abell 2744, and by  $z = 0$ , it will grow to a  $\sim 10^{16} M_{\odot}$  supercluster ([Jauzac et al. 2018](#)).

Of the four core subhalos, whose giant elliptical galaxy concentrations are denoted A, B, C and D by [Ma et al. \(2009\)](#), the overdensity of UDGs we detect in the upper portion of the WFC3 coverage appears to be possibly spatially associated with subhalo B. The NFW fit positions of the mass peaks from [Limousin et al. \(2016\)](#) associated with these light peaks are marked in Figure 8. Because of its undisturbed cool core, subhalo B is thought to be on its first infall into the cluster at a relative velocity of  $3000 \text{ km s}^{-1}$  ([Ma et al. 2009](#)). The UCDs, on the other hand, are concentrated near the southeast BCG.

In clusters with uneven spatial distributions of UDGs, we find tentative associations between UDGs and detected substructures in the clusters, often on their first infall. This is in stark contrast to Coma, where the UDGs are concentrated around the cluster centre and are thus likely longtime cluster members ([Koda et al. 2015](#)). Only in the most relaxed FF cluster do we find similar behaviour. The fact that UDGs are found in groups and the



near-linear UDG abundance halo-mass relation discussed above suggest that UDGs are not only formed in clusters, but are also formed outside and fall in. Coma and Abell S1063 demonstrate that many UDGs survive the relaxation of substructures to become mixed throughout clusters, save the densest regions. In their dissection of the Virgo Cluster, [Binggeli et al. \(1987\)](#) find different spatial distributions for the various morphological types. In particular, they find that bright dwarf elliptical (dE) galaxies are more concentrated than faint ones, and an even stronger effect is seen where nucleated dwarfs are more concentrated than non-nucleated ones. They also find that the radial number density profiles of dEs are well fitted by either exponential or King profiles, with no deficiency at the centre. Recall that many objects that perhaps would now be classified as UDGs are not a separate morphological class in that analysis, and are instead included with the dEs.

The ongoing Beyond Ultra-deep Frontier Fields And Legacy Observations (BUFFALO) will triple the ACS coverage for each cluster and quadruple the WFC3 coverage. The increased coverage will permit study of additional substructures that are just missed by the currently available WFC3 data and nearly fill in the regions between the cluster and parallel fields.

#### 4.4. UDGs as possible UCD factories?

There is growing evidence that the centres of galaxy clusters are destructive to UDGs, with lower mass UDGs particularly susceptible (e.g. [van der Burg et al. 2016](#); [Sales et al. 2019](#)). There are hints that low-mass UDGs may host particularly massive GCs (e.g. NGC1052-DF2, [van Dokkum et al. 2018](#)) that are UCD-like in their luminosities, but it is far too early to say if this holds for the entire population of such systems. Two UDGs in the Virgo cluster, VLSB-A and VLSB-D, are possibly undergoing such a tidal disruption ([Mihos et al. 2017](#); [Toloba et al. 2018](#)). In the FFs, we find that  $\sim 15\%$  of UDGs are either nucleated or host nearby compact systems that could survive the destruction of their hosts. Half of all UDGs with nuclei or point sources are found in the most relaxed cluster, Abell S1063, with the individual fractions ranging from 4% in MACS 0717 to 25% in Abell S1063, suggesting that perhaps their formation is tied to the relaxation of clusters. And recall that all point sources detected in the FFs are far too luminous to be GCs, with GCs in the nearest FF cluster having apparent magnitudes  $m_{814} \gtrsim 31$  mag. Nucleated dwarfs are also more concentrated in clusters ([Binggeli et al. 1987](#)), suggesting that the formation of a nucleus is tied to denser cluster environments. In Coma, over 50% of UDGs host nuclei ([Yagi et al. 2016](#)). It is possible that this fraction has evolved significantly since  $z \sim 0.4$ , but observational biases cannot be ruled out, with faint nuclei almost certainly being missed at the distances to the FF clusters.

In all of the FF clusters—but especially in Abell 2744 and Abell 370—the spatial distributions of UDGs and UCDs appear nearly opposite (see Figure 8). This observation was confirmed by running a 2D Kolmogorov-Smirnov test ([Press et al. 1992](#)) comparing the positions of UDGs and UCDs in each cluster field, and in each case, the differences between the spatial distributions of UDGs

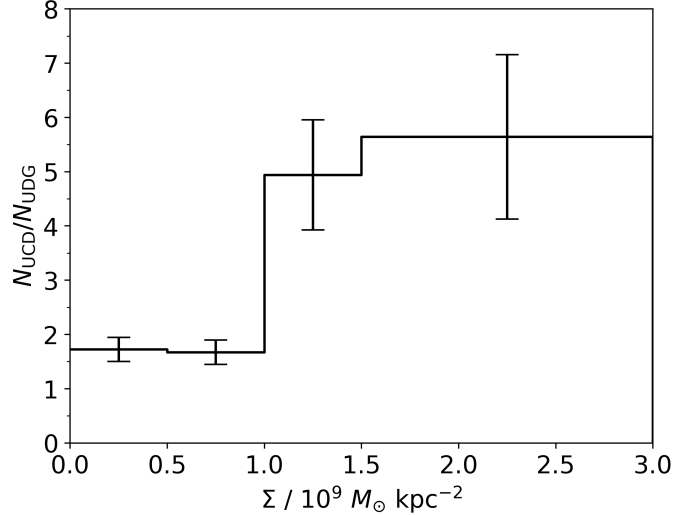


**Figure 10.** The ratio of UCDs to UDGs in bins of mass surface density across all six FF clusters. A single bin for mass surface densities greater than  $1.5 \times 10^9 M_\odot \text{ kpc}^{-2}$  was used due to the small areas of the clusters with such high densities. For each UDG and UCD, we used the wide-field low-resolution Merten lensing models ([Merten et al. 2009, 2011](#); [Zitrin et al. 2009, 2013](#)) to compute the mass surface density at its location. The abundance of UCDs relative to UDGs roughly triples in the high density regions of the clusters.

and UCDs are confirmed to be statistically significant.<sup>9</sup>

A different attempt to quantify this phenomenon was made by looking at the ratios of UDGs and UCDs as a function of environment. The measure of environment we chose was the gravitational lensing mass surface density since global tides are thought to drive the destruction of UDGs ([Sales et al. 2019](#)). The normalized mass surface density  $\kappa$ , or convergence, was looked up at the location of each galaxy using the wide-field  $\sim 10''$  resolution Merten maps. The physical mass surface density  $\Sigma$  was then computed by multiplying  $\kappa$  by the critical density, defined as

$$\Sigma_{\text{crit}} = \frac{c^2}{4\pi G} \frac{D_S}{D_L D_{LS}}. \quad (4)$$

The  $D$ 's above are angular diameter distances, where  $D_S$  is the distance to the source being lensed,  $D_L$  is the distance to the lens (cluster), and  $D_{LS}$  is the distance from the lens to the source behind it,  $D_{LS} = D_S - D_L$  ([Kneib, & Natarajan 2011](#)). The convergence maps are scaled such that  $D_{LS}/D_S = 1$ , and thus the dependence on the redshifts of the sources used to construct the maps is already taken into account. In Figure 10, we plot the ratio of UCDs to UDGs in bins of mass surface density across all six clusters. With only a small fraction of the area of the clusters exhibiting mass densities greater than  $1.5 \times 10^9 M_\odot \text{ kpc}^{-2}$ , a single bin was used for mass densities exceeding this. The ratio of UCDs to UDGs triples in regions of mass density greater than  $\Sigma = 1 \times 10^9 M_\odot \text{ kpc}^{-2}$ .

The only cluster without an excess of UCD candidates in the cluster field compared to the parallel field is MACS 1149. This cluster also fails to show a concentration of UCDs in proximity to the BCG. While MACS 1149 is one of the most distant FF clusters, limit-

<sup>9</sup> The highest  $p$ -value is 0.03 for both Abell 370 and MACS 1149, the lowest is  $4.6 \times 10^{-9}$  for Abell 2744.

ing us to the brightest UCDs, this behaviour is not seen in MACS 0717 at a nearly identical redshift. MACS 1149 presents with the faintest BCG and the least ICL (see Figure 8). It is the only cluster for which the radial distribution of UDGs plateaus towards the BCG.<sup>10</sup> Since tidal disruption of galaxies is thought to form the ICL (e.g. Burke et al. 2012), we speculate that MACS 1149 has a weaker tidal field than the other FF clusters, permitting UDGs to survive down to lower radii. This may then explain the low abundance of UCDs in MACS 1149 if the disruption of UDGs (or dwarf galaxies in general) are an important formation channel for UCDs. If this hypothesis is confirmed, it may then be possible to use the spatial distribution of UDGs and UCDs as tracers of the global cluster potential.

## 5. CONCLUSIONS

In this paper, we investigate the UDGs and UCDs inhabiting the six FF clusters—Abell 2744, MACSJ0416.1–2403, MACSJ0717.5+3745, MACSJ1149.5+2223, Abell S1063 and Abell 370—and their relation to each other and other structures present in the clusters. The results of this paper are as follows:

1. The six FF clusters are the most massive and distant ( $0.308 < z < 0.545$ ) clusters in which UDGs have been found, with each cluster hosting between  $\sim 200$  to  $\sim 1400$  UDGs. The total number of UDGs in these clusters is consistent with the abundance halo-mass relation defined at  $z \sim 0.05$  in groups and less massive clusters. The slope of the relation is weakly non-linear ( $N_{\text{UDG}} \propto [M_{200}]^{1.13}$ ) at the  $2\sigma$  level. With a slope above unity, it is possible that UDGs are more easily destroyed in low-mass halos and/or that UDGs may be created in clusters.
2. We find that UDGs tend to not be distributed uniformly in the cluster core fields. Only in the most relaxed FF cluster, Abell S1063, is the projected spatial distribution consistent with a uniform distribution. In at least some of the clusters, UDGs may be associated with known substructures late in their first infall and cluster merger events.
3. The locations of UDGs and UCDs appear anti-correlated. UCDs are abundant in the densest environments whereas UDGs are deficient towards the centres of galaxy clusters. The ratio of UCDs

to UDGs increases by roughly a factor of 3 from the lowest mass density regions of the clusters to the highest. It is interesting that MACS 1149 has the least amount of ICL and the faintest BCG, along with the lowest abundance of UCDs. Since tidal disruption of low-mass galaxies is responsible for building the ICL, we hypothesize that this is also responsible for producing UCDs. With many UDGs hosting compact sources, the destruction of UDGs in dense cluster environments may be an important formation channel of UCDs.

We thank NSERC for financial support, and acknowledge support from the NSF (AST-1616595, AST-1518294, AST-1515084 and AST-1616710). DAF thanks the ARC for financial support via DP130100388 and DP160101608. AJR was supported as a Research Corporation for Science Advancement Cottrell Scholar.

Based on observations made with the NASA/ESA *Hubble Space Telescope*, obtained from the data archive at the Space Telescope Science Institute, and associated with the Frontier Fields program.

STScI is operated by the Association of Universities for Research in Astronomy, Inc. under NASA contract NAS 5-26555.

This work utilizes gravitational lensing models produced by PIs Brada, Natarajan & Kneib (CATS), Merten & Zitrin, Sharon, Williams, Keeton, Bernstein and Diego, and the GLAFIC group. This lens modeling was partially funded by the HST Frontier Fields program conducted by STScI. STScI is operated by the Association of Universities for Research in Astronomy, Inc. under NASA contract NAS 5-26555. The lens models were obtained from the Mikulski Archive for Space Telescopes (MAST).

The scientific results reported in this article are based in part on data obtained from the *Chandra* Data Archive.

This research made use of Astropy,<sup>11</sup> a community-developed core Python package for Astronomy (Astropy Collaboration et al. 2013, 2018).

This research has made use of the NASA/IPAC Extragalactic Database (NED), which is operated by the Jet Propulsion Laboratory, California Institute of Technology, under contract with the National Aeronautics and Space Administration.

This research has made use of NASAs Astrophysics Data System Bibliographic Services.

Facilities: HST (ACS, WFC3), CXO

## APPENDIX

### LOPSIDEDNESS OF THE UDG DISTRIBUTION IN THE PARALLEL FIELDS

In Figure 11, we show the results of the same ‘lopsidedness’ test described in §4.3 and Figure 9, but now for the six parallel fields. In contrast to the cluster core fields, where only one cluster has a spatial distribution of UDGs consistent with being evenly distributed around the cluster centre, UDGs in the parallel fields are much more evenly distributed.

### ARTIFICIAL STAR TESTS

Artificial stars were used to test the completeness of our point source detection. A total of 50,000 artificial stars (in batches of 10,000) were injected into each of the cluster and parallel field *F814W* images at random positions with total magnitudes chosen uniformly from the range  $27 < m < 30.5$ . At each position, the PSFEX model was scaled to

<sup>10</sup> The radial distribution of UDGs also plateaus towards the centre of MACS 0717, but there the centre is not coincident with a BCG.

<sup>11</sup> <http://www.astropy.org>

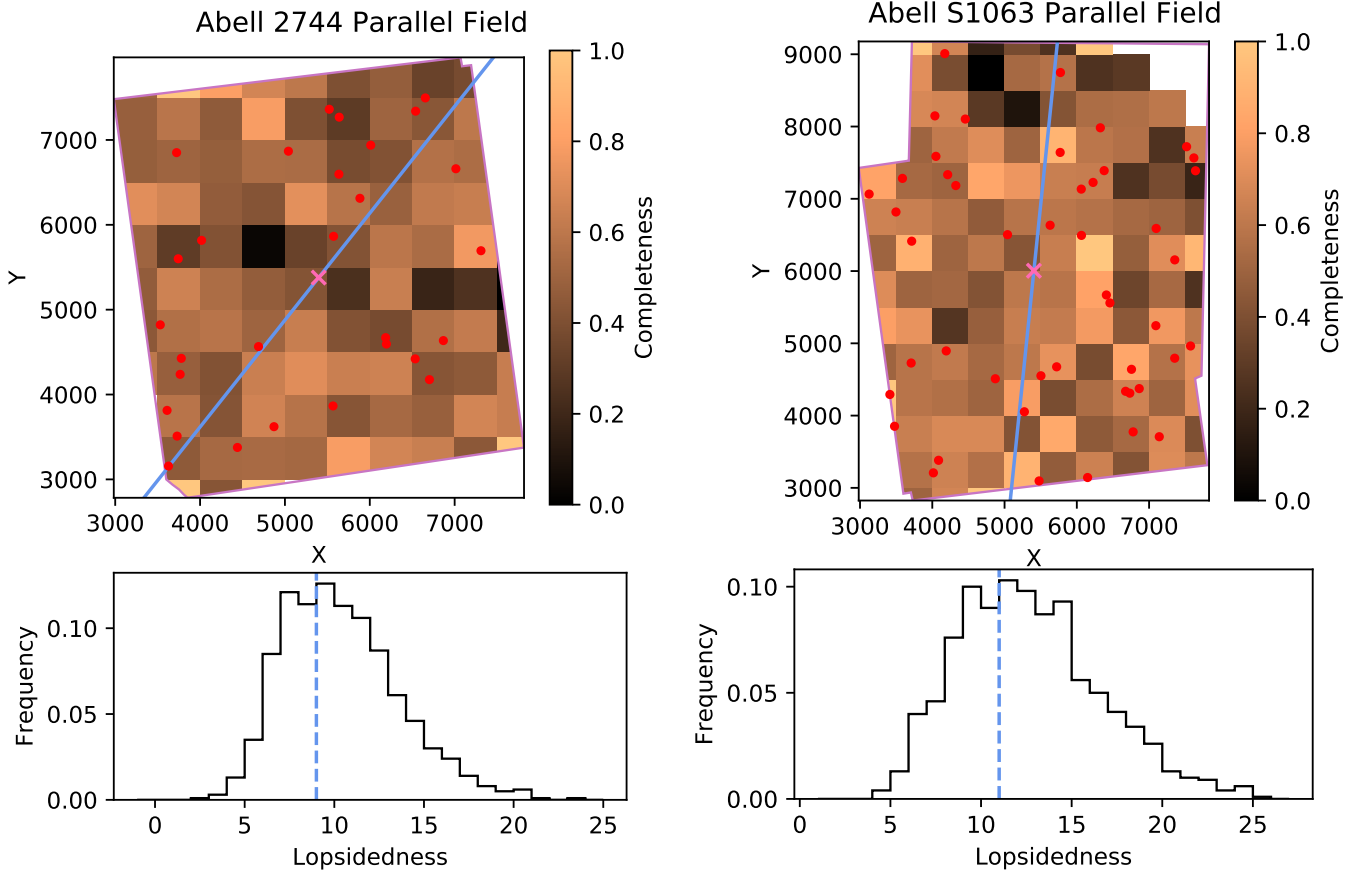


**Figure 11.** Same as Figure 9 but for the parallel fields.

match the desired magnitude in a 4 pixel diameter aperture. In Figure 12, the fraction of artificial stars detected is plotted in bins of injected magnitude. The completeness is modeled using the function

$$f(m) = \frac{1}{1 + e^{\alpha(m-m_{50})}}, \quad (\text{B1})$$

where  $m_{50}$  is the magnitude at which the completeness falls to 50% and  $\alpha$  determines how steep the completeness drops off (Harris et al. 2016). This simple parameterization is a much better description of the completeness behaviour in the parallel fields than in the cluster core fields, where the large galaxies and the ICL begin picking away at the completeness at magnitudes well below  $m_{50}$ . However, the estimate obtained for  $m_{50}$  is more than adequate. These results agree with the FF  $5\sigma$  point source depths of  $\sim 29$  AB magnitude reported by Lotz et al. (2017). Figure 13 shows the accuracy of recovered magnitudes.

## REFERENCES

- Agertz, O., & Kravtsov, A. V. 2016, *ApJ*, 824, 79  
 Alabi, A., Ferré-Mateu, A., Romanowsky, A. J., et al. 2018, *MNRAS*, 479, 3308  
 Amorisco, N. C., & Loeb, A. 2016, *MNRAS*, 459, L51  
 Amorisco, N. C., Monachesi, A., Agnello, A., et al. 2018, *MNRAS*, 475, 4235  
 Astropy Collaboration, Robitaille, T. P., Tollerud, E. J., et al. 2013, *A&A*, 558, A33  
 Astropy Collaboration, Price-Whelan, A. M., Sipőcz, B. M., et al. 2018, *AJ*, 156, 123  
 Balestra, I., Mercurio, A., Sartoris, B., et al. 2016, *ApJS*, 224, 33  
 Beasley, M. A., Romanowsky, A. J., Pota, V., et al. 2016, *ApJL*, 819, L20  
 Beasley, M. A., & Trujillo, I. 2016, *ApJ*, 830, 23  
 Bekki, K., Couch, W. J., Drinkwater, M. J., & Shioya, Y. 2003, *MNRAS*, 344, 399  
 Bertin, E., & Arnouts, S. 1996, *A&AS*, 117, 393  
 Bertin, E. 2011, *Astronomical Data Analysis Software and Systems XX*, 442, 435  
 Binggeli, B., Sandage, A., & Tammann, G. A. 1985, *AJ*, 90, 1681  
 Binggeli, B., Tammann, G. A., & Sandage, A. 1987, *AJ*, 94, 251  
 Bothun, G. D., Impey, C. D., & Malin, D. F. 1991, *ApJ*, 376, 404  
 Bradac, M., Huang, K.-H., Castellano, M., et al. 2019, *arXiv:1906.01725*  
 Brodie, J. P., Romanowsky, A. J., Strader, J., & Forbes, D. A. 2011, *AJ*, 142, 199  
 Burke, C., Collins, C. A., Stott, J. P., et al. 2012, *MNRAS*, 425, 2058  
 Burkert, A. 2017, *ApJ*, 838, 93  
 Butcher, H., & Oemler, A. 1978, *ApJ*, 219, 18  
 Butcher, H., & Oemler, A. 1984, *ApJ*, 285, 426  
 Caldwell, N. 1983, *AJ*, 88, 804  
 Caldwell, N., Armandroff, T. E., Da Costa, G. S., & Seitzer, P. 1998, *AJ*, 115, 535  
 Castellano, M., Amorín, R., Merlin, E., et al. 2016, *A&A*, 590, A31  
 Chabrier, G. 2003, *PASP*, 115, 763  
 Chan, T. K., Kereš, D., Wetzel, A., et al. 2018, *MNRAS*, 478, 906  
 Chen, C.-W., Côté, P., West, A. A., et al. 2010, *ApJS*, 191, 1  
 Dalcanton, J. J., Spergel, D. N., Gunn, J. E., et al. 1997, *AJ*, 114, 635  
 Danieli, S., van Dokkum, P., Conroy, C., et al. 2019, *ApJL*, 874, L12  
 Di Cintio, A., Brook, C. B., Dutton, A. A., et al. 2017, *MNRAS*, 466, L1



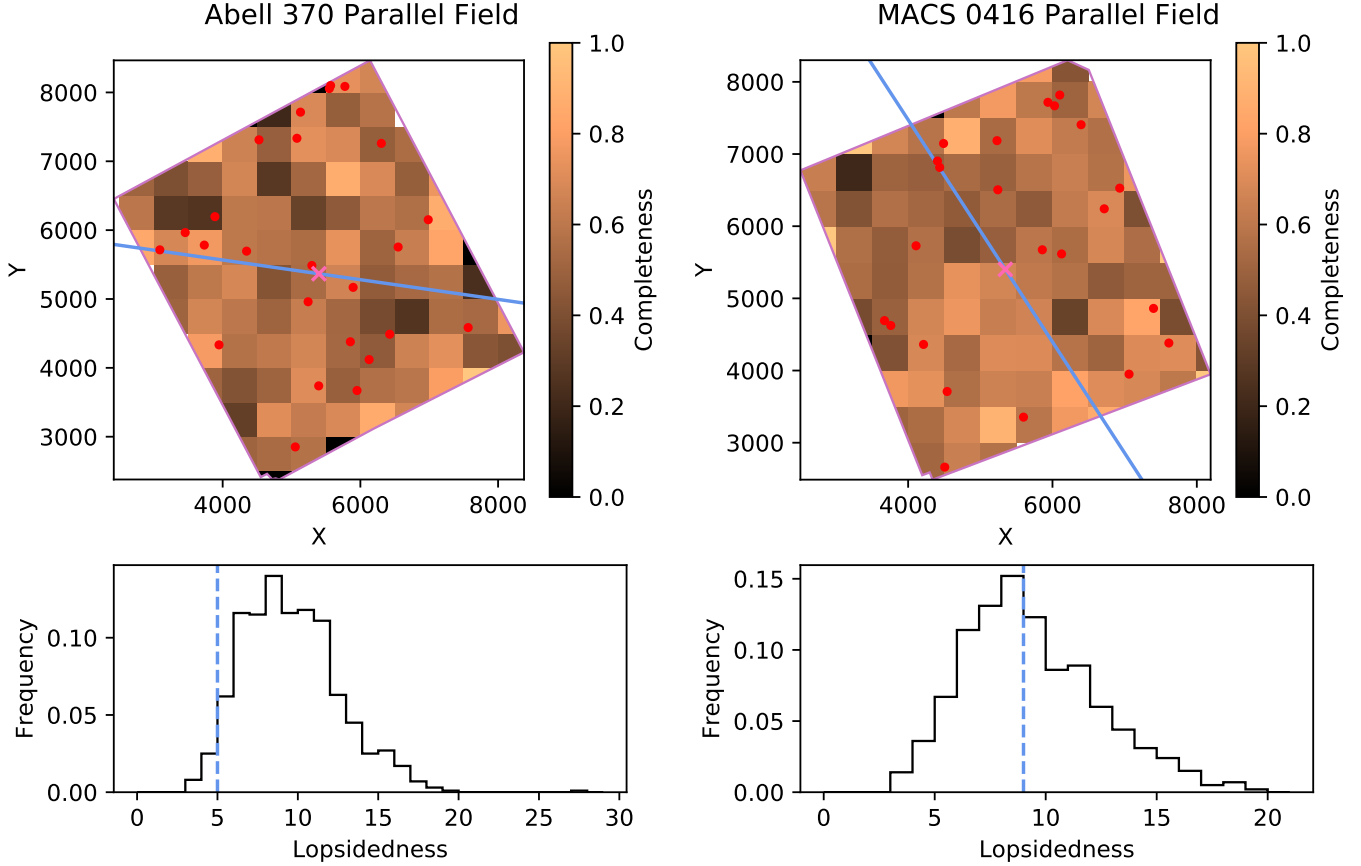


**Figure 11.** (Continued.)

Diego, J. M., Broadhurst, T., Wong, J., et al. 2016, *MNRAS*, 459, 3447

Dressler, A., Oemler, A., Butcher, H. R., et al. 1994, *ApJ*, 430, 107

Drinkwater, M. J., Gregg, M. D., & Colless, M. 2001, *ApJL*, 548, L139

Ebeling, H., Barrett, E., & Donovan, D. 2004, *ApJL*, 609, L49

Ebeling, H., Barrett, E., Donovan, D., et al. 2007, *ApJL*, 661, L33

Edge, A. C., Ebeling, H., Bremer, M., et al. 2003, *MNRAS*, 339, 913

Ferguson, H. C., & Sandage, A. 1988, *AJ*, 96, 1520

Ferré-Mateu, A., Alabi, A., Forbes, D. A., et al. 2018, *MNRAS*, 479, 4891

Forbes, D. A., Norris, M. A., Strader, J., et al. 2014, *MNRAS*, 444, 2993

Golovich, N., Dawson, W. A., Wittman, D., et al. 2016, *ApJ*, 831, 110

Gómez, P. L., Valkonen, L. E., Romer, A. K., et al. 2012, *AJ*, 144, 79

Graham, A. W., & Driver, S. P. 2005, *PASA*, 22, 118

Gruen, D., Brimiouille, F., Seitz, S., et al. 2013, *MNRAS*, 432, 1455

Harris, W. E., Blakeslee, J. P., Whitmore, B. C., et al. 2016, *ApJ*, 817, 58

Harris, K. A., Debattista, V. P., Governato, F., et al. 2017, *MNRAS*, 467, 4501

Illingworth, G. D., Magee, D., Oesch, P. A., et al. 2013, *ApJS*, 209, 6

Impey, C., Bothun, G., & Malin, D. 1988, *ApJ*, 330, 634

Janssens, S., Abraham, R., Brodie, J., et al. 2017, *ApJL*, 839, L17

Janz, J., Norris, M. A., Forbes, D. A., et al. 2016, *MNRAS*, 456, 617

Jauzac, M., Jullo, E., Kneib, J.-P., et al. 2012, *MNRAS*, 426, 3369

Jauzac, M., Jullo, E., Eckert, D., et al. 2015, *MNRAS*, 446, 4132

Jauzac, M., Eckert, D., Schwinn, J., et al. 2016, *MNRAS*, 463, 3876

Jauzac, M., Eckert, D., Schaller, M., et al. 2018, *MNRAS*, 481, 2901

Jiang, F., Dekel, A., Freundlich, J., et al. 2019, *MNRAS*, 487, 5272

Johnson, T. L., Sharon, K., Bayliss, M. B., et al. 2014, *ApJ*, 797, 48

Kneib, J.-P., & Natarajan, P. 2011, *A&A Rev.*, 19, 47.

Koda, J., Yagi, M., Yamanoi, H., & Komiyama, Y. 2015, *ApJL*, 807, L2

Koekemoer, A. M., Faber, S. M., Ferguson, H. C., et al. 2011, *ApJS*, 197, 36

Lagattuta, D. J., Richard, J., Clément, B., et al. 2017, *MNRAS*, 469, 3946

Lagattuta, D. J., Richard, J., Bauer, F. E., et al. 2019, *MNRAS*, 485, 3738

Leisman, L., Haynes, M. P., Janowiecki, S., et al. 2017, *ApJ*, 842, 133

Liao, S., Gao, L., Frenk, C. S., et al. 2019, *arXiv:1904.06356*

Limousin, M., Ebeling, H., Richard, J., et al. 2012, *A&A*, 544, A71

Limousin, M., Richard, J., Jullo, E., et al. 2016, *A&A*, 588, A99

Lotz, J. M., Koekemoer, A., Coe, D., et al. 2017, *ApJ*, 837, 97

Ma, C.-J., Ebeling, H., & Barrett, E. 2009, *ApJ*, 693, L56

Mancera Piña, P. E., Peletier, R. F., Aguerri, J. A. L., et al. 2018, *MNRAS*, 481, 4381

Mancone, C. L., & Gonzalez, A. H. 2012, *PASP*, 124, 606

Mann, A. W., & Ebeling, H. 2012, *MNRAS*, 420, 2120

Martin, G., Kaviraj, S., Laigle, C., et al. 2019, *MNRAS*, 485, 796

Martín-Navarro, I., Romanowsky, A. J., Brodie, J. P., et al. 2019, *MNRAS*, 484, 3425

Martínez-Delgado, D., Läsker, R., Sharina, M., et al. 2016, *AJ*, 151, 96

Medezinski, E., Umetsu, K., Nonino, M., et al. 2013, *ApJ*, 777, 43

Medezinski, E., Umetsu, K., Okabe, N., et al. 2016, *ApJ*, 817, 24

Merlin, E., Amorín, R., Castellano, M., et al. 2016, *A&A*, 590, A30

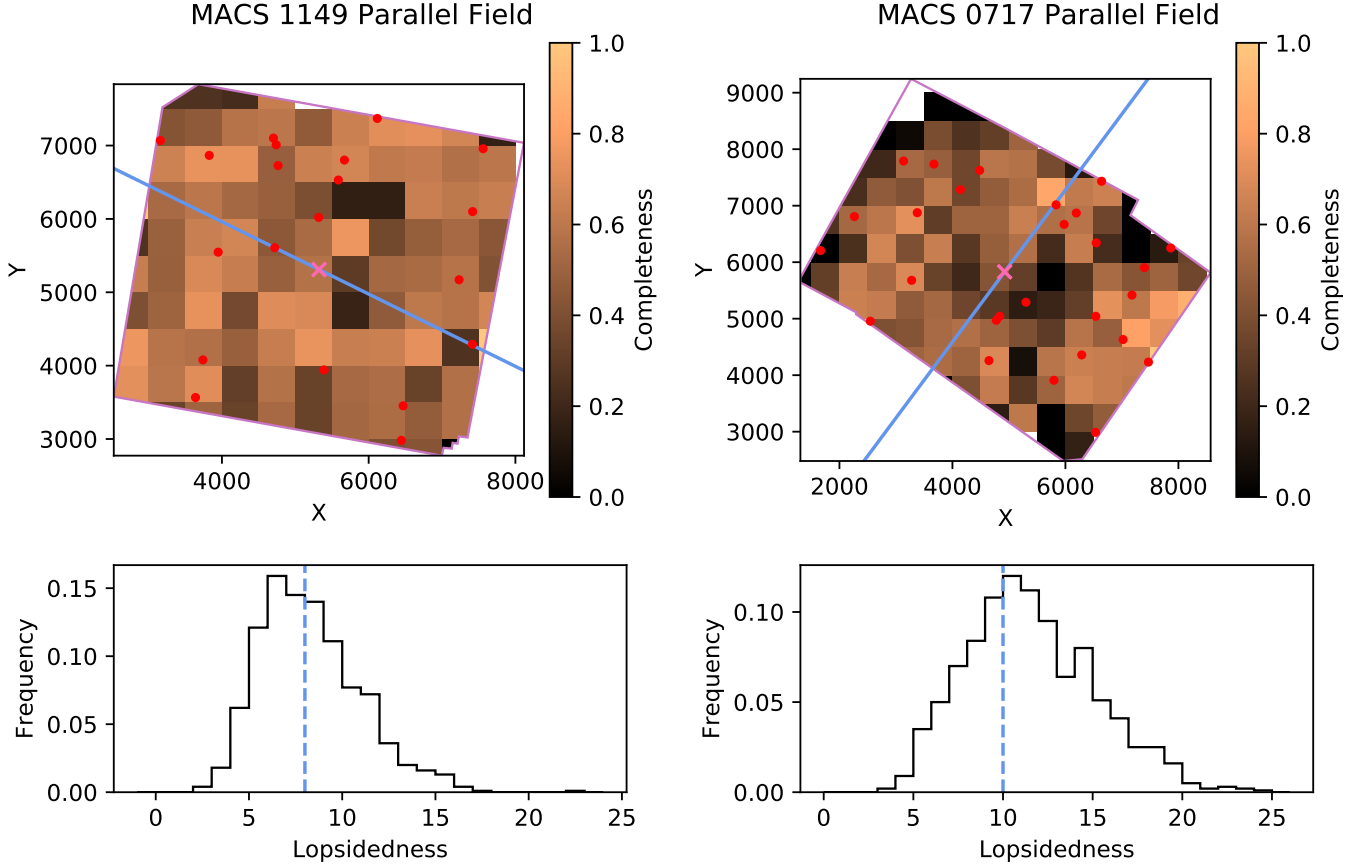
Merten, J., Cacciato, M., Meneghetti, M., Mignone, C., & Bartelmann, M. 2009, *A&A*, 500, 681

Merten, J., Coe, D., Dupke, R., et al. 2011, *MNRAS*, 417, 333

Mihos, J. C., Harding, P., Feldmeier, J. J., et al. 2017, *ApJ*, 834, 16

Moore, B., Lake, G., & Katz, N. 1998, *ApJ*, 495, 139

Muñoz, R. P., Eigenthaler, P., Puzia, T. H., et al. 2015, *ApJL*, 813, L15

**Figure 11.** (Continued.)

- Norris, M. A., Kannappan, S. J., Forbes, D. A., et al. 2014, *MNRAS*, 443, 1151
- Ogrea, G. A., van Weeren, R. J., Jones, C., et al. 2015, *ApJ*, 812, 153
- Owers, M. S., Randall, S. W., Nulsen, P. E. J., et al. 2011, *ApJ*, 728, 27
- Peng, C. Y., Ho, L. C., Impey, C. D., & Rix, H.-W. 2002, *AJ*, 124, 266
- Peng, E. W., & Lim, S. 2016, *ApJL*, 822, L31
- Pfeffer, J., & Baumgardt, H. 2013, *MNRAS*, 433, 1997
- Press, W. H., Teukolsky, S. A., Vetterling, W. T., et al. 1992, Cambridge: University Press
- Rafelski, M., Teplitz, H. I., Gardner, J. P., et al. 2015, *AJ*, 150, 31
- Redlich, M., Bartelmann, M., Waizmann, J.-C., et al. 2012, *A&A*, 547, A66
- Reines, A. E., Greene, J. E., & Geha, M. 2013, *ApJ*, 775, 116
- Richard, J., Kneib, J.-P., Limousin, M., et al. 2010, *MNRAS*, 402, L44
- Richard, J., Jauzac, M., Limousin, M., et al. 2014, *MNRAS*, 444, 268
- Román, J., & Trujillo, I. 2017a, *MNRAS*, 468, 703
- Román, J., & Trujillo, I. 2017b, *MNRAS*, 468, 4039
- Rong, Y., Guo, Q., Gao, L., et al. 2017, *MNRAS*, 470, 4231
- Rong, Y., Dong, X.-Y., Puzia, T. H., et al. 2019, *arXiv:1907.10079*
- Sales, L. V., Navarro, J. F., Penafiel, L., et al. 2019, *arXiv:1909.01347*
- Schlafly, E. F., & Finkbeiner, D. P. 2011, *ApJ*, 737, 103
- Sandage, A., & Binggeli, B. 1984, *AJ*, 89, 919
- Silk, J. 2019, *MNRAS*, L105
- Sirianni, M., Jee, M. J., Benítez, N., et al. 2005, *PASP*, 117, 1049
- Toloba, E., Lim, S., Peng, E., et al. 2018, *ApJL*, 856, L31
- Tremmel, M., Wright, A. C., Brooks, A. M., et al. 2019, *arXiv:1908.05684*
- Umetsu, K., Broadhurst, T., Zitrin, A., et al. 2011, *ApJ*, 729, 127
- Umetsu, K., Zitrin, A., Gruen, D., et al. 2016, *ApJ*, 821, 116
- van der Burg, R. F. J., Muzzin, A., & Hoekstra, H. 2016, *A&A*, 590, A20
- van der Burg, R. F. J., Hoekstra, H., Muzzin, A., et al. 2017, *A&A*, 607, A79
- van der Wel, A., Bell, E. F., Häussler, B., et al. 2012, *ApJS*, 203, 24
- van Dokkum, P. G., Abraham, R., Merritt, A., et al. 2015, *ApJL*, 798, L45
- van Dokkum, P., Abraham, R., Brodie, J., et al. 2016, *ApJL*, 828, L6
- van Dokkum, P., Danieli, S., Cohen, Y., et al. 2018a, *Nature*, 555, 629
- van Dokkum, P., Cohen, Y., Danieli, S., et al. 2018b, *ApJL*, 856, L30
- van Dokkum, P., Danieli, S., Abraham, R., et al. 2019a, *ApJL*, 874, L5
- van Dokkum, P., Wasserman, A., Danieli, S., et al. 2019b, *ApJ*, 880, 91
- Yagi, M., Koda, J., Komiyama, Y., & Yamanai, H. 2016, *ApJS*, 225, 11
- Yozin, C., & Bekki, K. 2015, *MNRAS*, 452, 937
- Zitrin, A., Broadhurst, T., Umetsu, K., et al. 2009, *MNRAS*, 396, 1985
- Zitrin, A., Meneghetti, M., Umetsu, K., et al. 2013, *ApJL*, 762, L30

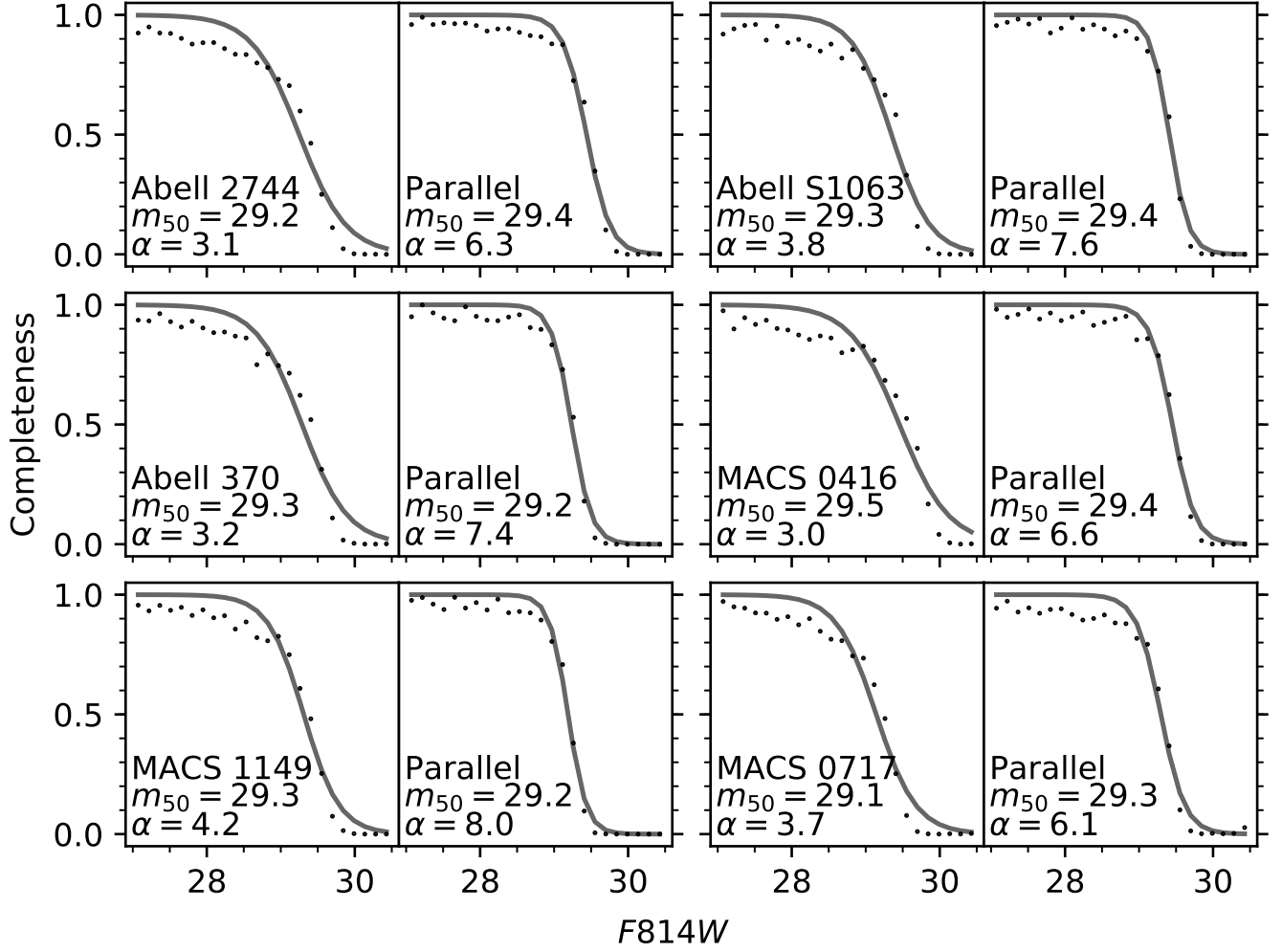


**Figure 12.** Fraction of artificial stars recovered in bins of injected magnitude for each of the cluster and parallel fields. The bins are 0.15 mag in size. The solid line is the best fit function of the form  $f(m) = (1 + \exp(\alpha(m - m_{50}))^{-1}$ , where  $m_{50}$  is the magnitude at which 50% of the sources are recovered and  $\alpha$  is the steepness at which the completeness drops off, both of which are listed in each panel.

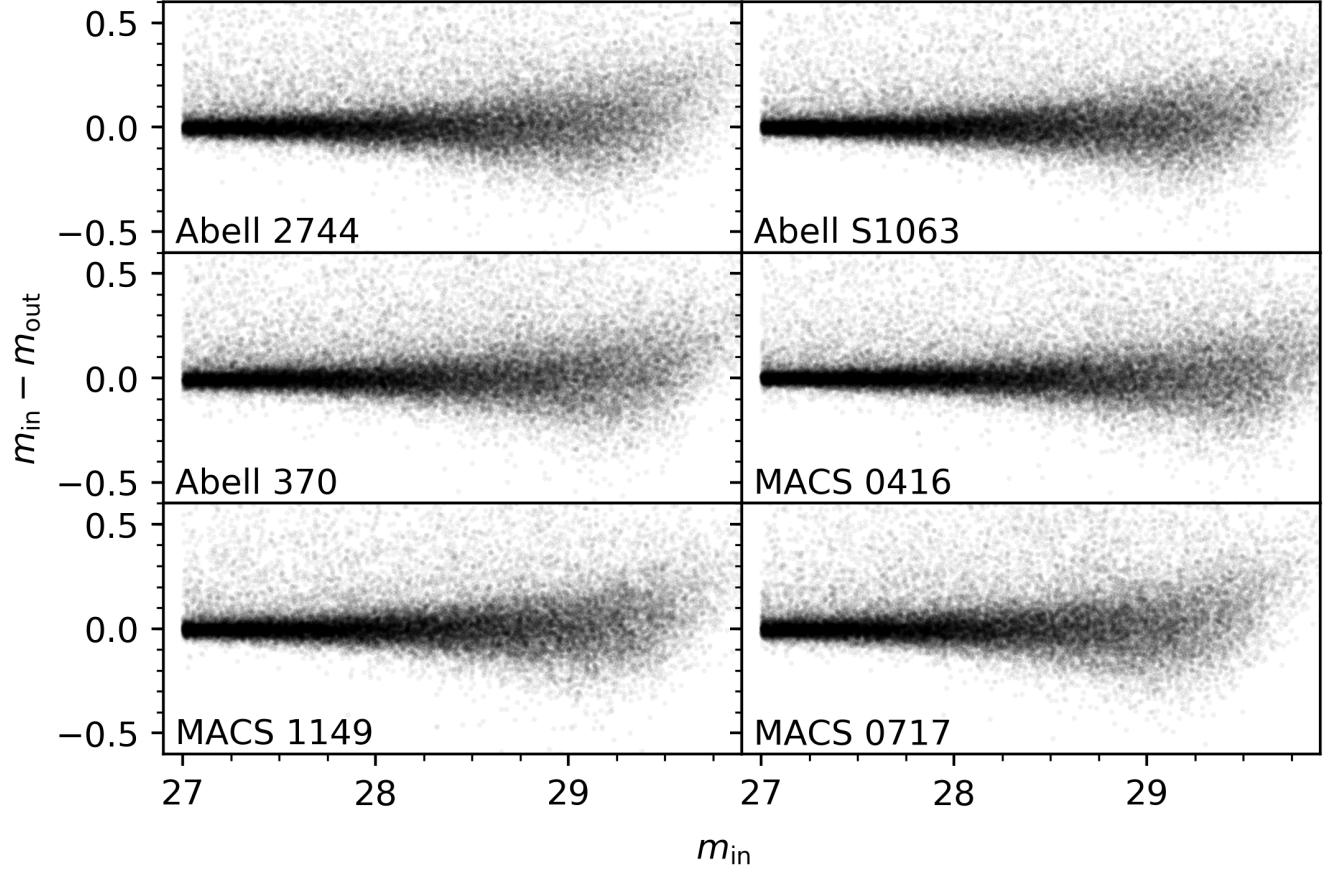


**Figure 13.** Difference between injected and recovered magnitudes for artificial stars.



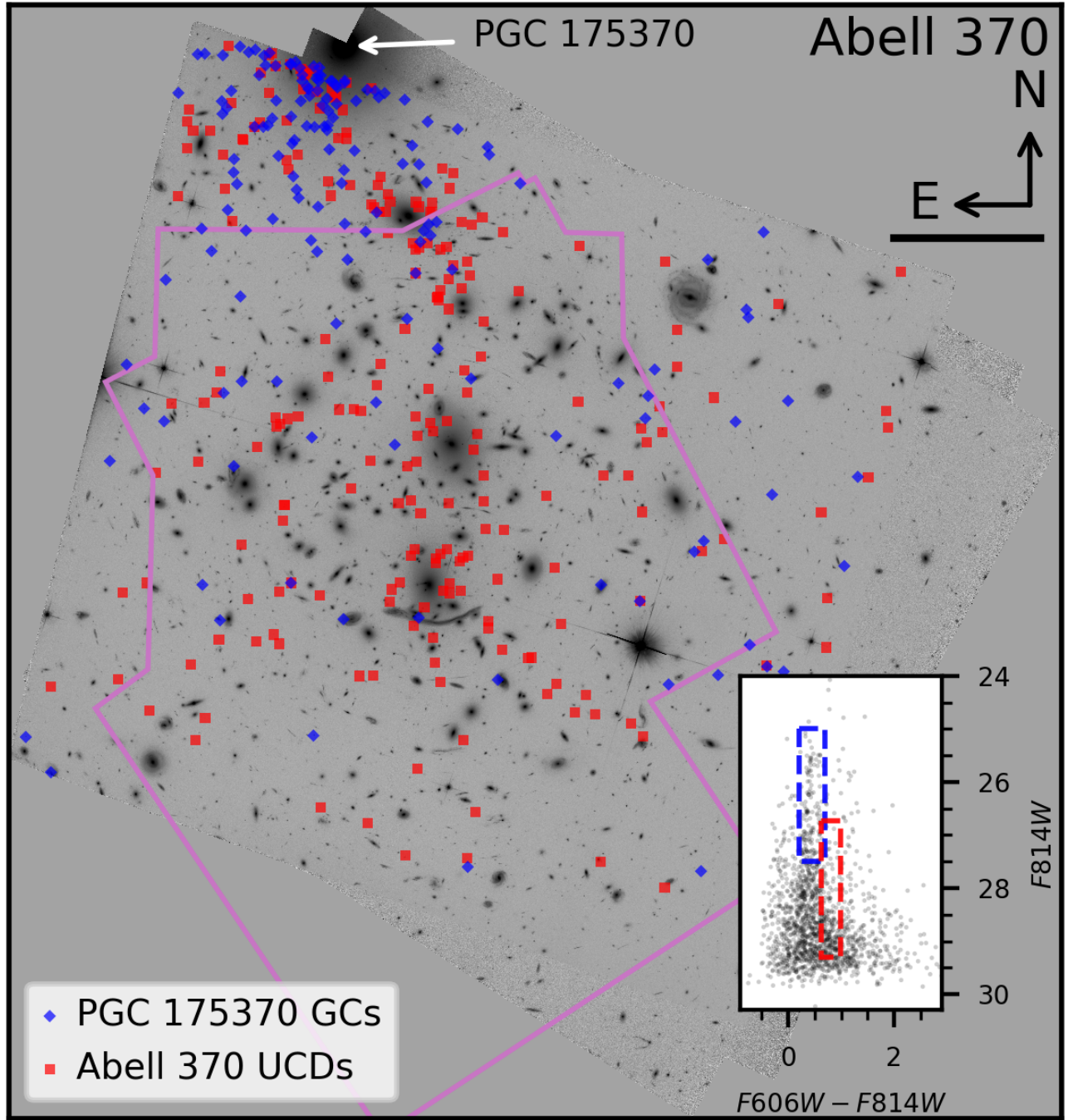


**Figure 14.** *F814W* image of Abell 370. The location of PGC 175370 is marked with the arrow. The black line below the compass measures 200 kpc in length. Marked in blue are globular cluster candidates likely belonging to the foreground galaxy PGC 175370. The foreground GC candidates are selected with the blue selection box in the inset CMD in the bottom right. Abell 370's UCD candidates are marked in red, selected using the red box in the CMD. In contrast to Figure 8, UCD selection was not limited to the WFC3 region, shown as the pink outline, but limiting our analysis to the WFC3 region removes the most likely contaminants.